Check for updates

JGR Atmospheres

RESEARCH ARTICLE
10.1029/2024JD043186

# Climate Feedbacks Derived From Spatial Gradients in Recent Climatology

**P. Goodwin[1], R. G. Williams[2], P. Ceppi[3], and B. B. Cael[4,5]**

[1]School of Ocean and Earth Science, University of Southampton, Southampton, UK, [2]Department of Earth, Ocean and Ecological Sciences, School of Environmental Sciences, University of Liverpool, Liverpool, UK, [3]Department of Physics, Imperial College London, London, UK, [4]Ocean Biogeosciences, National Oceanography Center, Southampton, UK, [5]Department of the Geophysical Sciences, University of Chicago, Chicago, IL, USA

**Key Points:**

- Earth's radiation budget is related to surface and atmospheric properties in recent climatology using simplified empirical relations
- Spatial variations in outgoing radiation are dominated by their dependence on surface temperature
- Climate feedbacks are evaluated spatially by differentiating the simplified empirical relations with respect to surface temperature

**Supporting Information:**

Supporting Information may be found in the online version of this article.

**Correspondence to:**

P. Goodwin,
p.a.goodwin@soton.ac.uk

**Citation:**

Goodwin, P., Williams, R. G., Ceppi, P., & Cael, B. B. (2025). Climate feedbacks derived from spatial gradients in recent climatology. *Journal of Geophysical Research: Atmospheres*, *130*, e2024JD043186. https://doi.org/10.1029/2024JD043186

Received 19 DEC 2024
Accepted 10 JUN 2025

**Author Contributions:**

**Conceptualization:** P. Goodwin
**Formal analysis:** P. Goodwin, R. G. Williams, P. Ceppi, B. B. Cael
**Methodology:** P. Goodwin
**Software:** P. Goodwin
**Writing – original draft:** P. Goodwin, R. G. Williams, P. Ceppi, B. B. Cael
**Writing – review & editing:** P. Goodwin, R. G. Williams, P. Ceppi, B. B. Cael

© 2025. The Author(s).
This is an open access article under the terms of the Creative Commons Attribution License, which permits use, distribution and reproduction in any medium, provided the original work is properly cited.

**Abstract** Climate feedbacks, including Planck, surface albedo, water vapor-lapse rate (WVLR) and cloud feedbacks, determine how much surface temperatures will eventually warm to balance anthropogenic radiative forcing. Climate feedbacks remain difficult to constrain directly from temporal variation in observed surface warming and radiation budgets due to the pattern effect and low signal-to-noise ratio, with only order 1°C historic rise in surface temperatures and high uncertainty in aerosol radiative forcing. This study presents a new method to analyze climate feedbacks from observations by empirically fitting simplified reduced-physics relations for outgoing radiation at the top of the atmosphere (TOA) to observed spatial variation in climate properties and radiation budgets. Spatial variations in TOA outgoing radiation are dominated by the dependence on surface temperature: around 91% of the spatial variation in clear sky albedo, and 77% of spatial variation in clear sky TOA outgoing longwave radiation, is functionally explained by variation in surface temperatures. These simplified and observationally constrained relations are then differentiated with respect to spatial contrasts in surface temperature to reveal the Planck, fixed-cloud albedo ($\lambda_{\text{albedo}}$) and WVLR ($\lambda_{\text{WVLR}}$) climate feedbacks spatially for both clear sky and all sky conditions. The resulting global all sky climate feedback values are $\lambda_{\text{WVLR}} = 1.28$ (1.13–1.45 at 66%) $\text{Wm}^{-2}\text{K}^{-1}$, and $\lambda_{\text{albedo}} = 0.64$ (0.53–0.74) $\text{Wm}^{-2}$ for the period 2003–2023, reducing to 0.35 (0.29–0.41) $\text{Wm}^{-2}\text{K}^{-1}$ under 4°C warming after cryosphere retreat. Our findings agree well with complex Earth system model evaluations based on temporal climate perturbations, and our approach is complementary.

**Plain Language Summary** The climate feedback measures how much Earth's surface temperatures will change in response to climate forcing from rising greenhouse gas concentrations. However, our observed record of surface temperature changes over time in response to rising greenhouse gas concentrations in the past is not long enough to accurately determine Earth's climate feedback for the future. In part, this limitation is because recent anthropogenic warming has only reached around 1 degree Celsius of temperature change globally so far. Here, we take an alternative approach: instead of considering how Earth's surface temperatures have changed over time we consider how Earth's surface temperatures change from the cold polar regions to the warm tropics which provides a much larger temperature change of around 80 degrees Celsius. By accounting for the different physical processes that affect Earth's surface temperature spatially, we are able to provide an estimate of the climate feedback in response to a climate forcing from greenhouse gas concentrations. Our spatial-change estimates of climate feedback are independent of the existing temporal-change estimates, but are in good agreement with current estimates of climate feedback.

## 1. Introduction

An imbalance in Earth's energy budget at the top of the atmosphere (TOA) is eventually restored through climate feedback processes, whereby an increase in surface temperatures leads to an increase in outgoing radiation at TOA. The total climate feedback from all processes, $\lambda_{\text{total}}$ in $\text{Wm}^{-2}\text{K}^{-1}$, is defined as minus the partial derivative of outgoing radiation at TOA, $R_{\text{out}}$ in $\text{Wm}^{-2}\text{K}^{-1}$, with respect to surface temperature, $T_S$ in K,

$$\lambda_{\text{total}} = -\frac{\partial R_{\text{out}}}{\partial T_S}. \quad (1)$$

21698996, 2025, 12, Downloaded from https://agupubs.onlinelibrary.wiley.com/doi/10.1029/2024JD043186 by Imperial College London, Wiley Online Library on [19/10/2026]. See the Terms and Conditions (https://onlinelibrary.wiley.com/terms-and-conditions) on Wiley Online Library for rules of use; OA articles are governed by the applicable Creative Commons License

$\lambda_{\text{total}}$ for the present day Earth system is an important quantity in global climate science, since it is inversely linked to the Equilibrium Climate Sensitivity (ECS), ECS $\sim 1/\lambda_{\text{total}}$, and so determines the future surface warming response to some specified anthropogenic forcing. This total climate feedback may be decomposed into individual climate feedbacks from different processes, $\lambda_{\text{total}} = \sum \lambda_X$, where the feedback from process $X$ is,

$$\lambda_X = -\frac{\partial R_{\text{out}}}{\partial T_S}\bigg|_{\delta X} = -\frac{\partial [S_{\text{out}} + L_{\text{out}}]}{\partial T_S}\bigg|_{\delta X} = -\frac{\partial [S_{\text{out}} + L_{\text{out}}]}{\partial X}\frac{\partial X}{\partial T_S}, \tag{2}$$

where $S_{\text{out}}$ is the outgoing shortwave radiation and $L_{\text{out}}$ is the outgoing longwave radiation at the TOA. The different climate feedback processes, $\lambda_X$, include the Planck feedback, the water vapor-lapse rate (WVLR) feedback, the surface albedo feedback, and cloud feedbacks; see Sherwood et al. (2020) for a comprehensive assessment.

Existing studies quantify climate feedbacks (either as the total feedback or the separate contributions from individual processes) through temporal changes in surface temperatures and Earth's energy budget at TOA using either observations, numerical simulations or paleoclimate archives (e.g., Sherwood et al., 2020). However, temporal observations have only a limited historic record, especially for the energy budget, and the observed anthropogenic warming signal of around 1K is relatively small in comparison to the interannual variability and the uncertainty of the radiative effects of aerosols (Sherwood et al., 2020). Moreover, the climate feedback may have had a different mean value in recent historic decades than it does now due to how changing patterns of surface warming over time alter climate feedback, known as the pattern effect (see e.g. Gregory and Andrews, 2016).

Climate feedbacks are readily evaluated from numerical climate model simulations (e.g., Soden et al., 2008; Zelinka et al., 2020), which can use idealized forcing without aerosol contributions and simulate a longer time period than the historic record. Although modern climate models include sophisticated representations of physical processes, the evaluated climate feedbacks do differ between different models (e.g., Zelinka et al., 2020), and so any single numerical model simulations may be biased relative to the real world. Also, if the goal is to evaluate the climate feedback contributions from different individual processes, $\lambda_X$, then the relatively large finite perturbations employed in numerical climate models lead to linear combination error in the individual feedbacks, such that $\lambda_{\text{total}} \neq \sum \lambda_X$ (e.g., the rms difference between $\lambda_{\text{total}}$ and $\sum \lambda_X$ is 17.2% for 27 CMIP6 models assessed by Zelinka et al., 2020%, and 17.7% for 28 CMIP5 models). Note that this nonlinear effect only impacts the values of $\lambda_X$ for each process and does not impact the value of the total climate feedback, $\lambda_{\text{total}}$.

Consider an alternative approach based on the spatial variation in TOA outgoing radiation and surface temperature (Figure 1). Evaluated with 1° horizontal resolution during the period 2003–2023, surface temperature correlates to TOA outgoing radiation and explains some 74% of the variance in TOA outgoing radiation (Figure 1), with a sensitivity of $\frac{\delta R_{\text{out}}}{\delta T_S} \approx 1.28\ \text{Wm}^{-2}\text{K}^{-1}$. This crude observational estimate is consistent in magnitude to recent estimates of climate feedback (e.g., $-\lambda_{\text{total}} = \partial R_{\text{out}}/\partial T_S = 1.30 \pm 0.44$ in Sherwood et al., 2020). However, it is not in general robust to assume that the value of $\delta R_{\text{out}}/\delta T_S$ analyzed spatially and the value of $\partial R_{\text{out}}/\partial T_S$ are similar: a significant part of the observed spatial variation in $R_{\text{out}}$ may arise from factors that co-vary in space with $T_S$ in recent climatology, but would not co-vary in time following a perturbation to the climate system. For example, Feng et al. (2023a, 2023b) reveal that some processes that contribute to how clear sky outgoing longwave radiation increases with surface temperature lead to a linear relationship (and so would also contribute in a similar manner spatially and temporally) but some processes lead to a departure from a linear relationship (and so would not act in a similar way temporally and spatially). These factors leading to departures from linearity, such as the mid-troposphere relative humidity (Feng et al., 2023b), should be accounted for before making inferences on climate feedback from spatial information.

Previous studies in the literature have successfully related TOA outgoing radiation to parameters describing atmospheric and surface properties, either empirically or theoretically (e.g., Ingram, 2010; Koll and Cronin, 2018; Raval and Ramanathan, 1989; Schmidt et al., 2010), and so have described combinations of processes and parameters that explain variation in $R_{\text{out}}$. However, in general these empirically fitted relations for $R_{\text{out}}$ are not easily differentiable with respect to surface temperature so cannot then be used to diagnose the climate feedback, Equation 1.

The goal of this study is to evaluate climate feedbacks from the Planck, WVLR and surface albedo feedback processes using observations of the *spatial* variation in TOA outgoing radiation, surface temperature and other

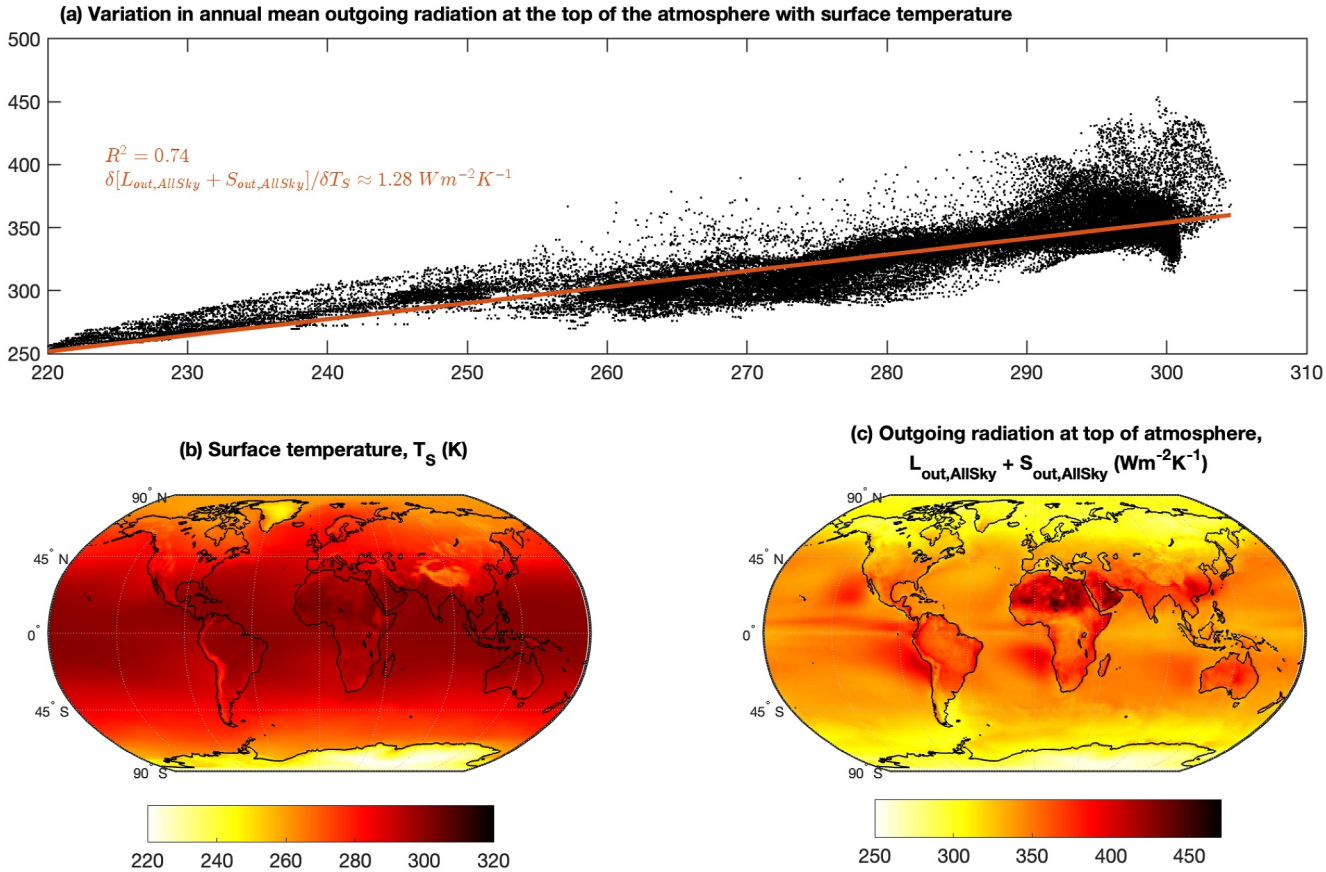



**Figure 1.** Spatial variation in total outgoing radiation correlating with surface temperature for the 2003–2023 period, analyzed as annual-mean climatology, with each dot (a) representing a single location with 1 deg by 1 deg horizontal resolution. Surface temperature (b) evaluated from ERA5 (Hersbach et al., 2023) and outgoing radiation (c) from EBAF4.2 (Loeb et al., 2018).

properties of the Earth's surface and atmosphere (where these other properties used in addition to surface temperature to help evaluate the climate feedbacks preferably vary independently of surface temperature). *Spatial* variation in observed surface temperature is of order 80 K (Figure 1), thus providing a better signal-to-noise ratio than the much smaller order 1K *temporal* variation in observed surface temperature. To evaluate climate feedbacks, we first empirically relate $R_{\text{out}}$ to $T_S$ and other atmospheric and surface properties using functional forms that are easily differentiable with respect to surface temperature. The analysis is conducted on a 1° by 1° spatial resolution using climatology for the period 2003–2023, evaluating feedbacks for both clear skies conditions and all skies conditions assuming constant cloud amount and cloud properties (i.e., fixed-cloud all sky conditions). Additional climate feedbacks associated with changes in cloud amount or cloud properties are not considered.

Recent studies have estimated climate feedbacks from theory and/or spatial variation in climate properties (e.g., Feldl & Merlis, 2023; Koll et al., 2023; Roemer et al., 2023). Feldl and Merlis (2023) use theory and spatial variation in climate properties to calculate climate feedback, but crucially the theory in their method does not solve for the radiative properties of the system, and instead employs radiative kernels (e.g., Soden et al., 2008) evaluated from model output forced with finite perturbations. Therefore, the Feldl and Merlis (2023) method does not provide an assessment of climate feedback terms that is independent of the numerical climate models. Koll et al. (2023) solves for a climate feedback term from first principles theoretically, and so does not require numerical model input, but solves for the longwave climate feedback under clear sky conditions only. The aim here is to solve for climate feedback terms involving Planck, WVLR and fixed-cloud albedo, each under both clear sky and all sky conditions, using theory applied to observational data for the climatological mean state. The climate feedbacks are solved independently of both numerical model output or time-varying climate signals. Note that fixed-cloud albedo includes both surface albedo and atmospheric albedo changes that are not caused by clouds (e.g., water vapor), whereas the WVLR feedback is explicitly a longwave-only feedback in this analysis.



21698996, 2025, 12, Downloaded from https://agupubs.onlinelibrary.wiley.com/doi/10.1029/2024JD043186 by Imperial College London, Wiley Online Library on [19/10/2026]. See the Terms and Conditions (https://onlinelibrary.wiley.com/terms-and-conditions) on Wiley Online Library for rules of use; OA articles are governed by the applicable Creative Commons License

21698996, 2025, 12, Downloaded from https://agupubs.onlinelibrary.wiley.com/doi/10.1029/2024JD043186 by Imperial College London, Wiley Online Library on [19/10/2026]. See the Terms and Conditions (https://onlinelibrary.wiley.com/terms-and-conditions) on Wiley Online Library for rules of use; OA articles are governed by the applicable Creative Commons License

Section 2 of this study derives and empirically fits new reduced physics, simplified relations describing variation in TOA outgoing radiation in terms of surface temperature and other surface and atmospheric properties. Section 3 then differentiates these simplified relations to evaluate the Planck, WVLR, and fixed-cloud albedo climate feedbacks under clear sky and all sky conditions.

## 2. Simplified Empirical Relations for Outgoing Radiation at the TOA

### 2.1. A Framework for TOA Outgoing Radiation, Planetary Emissivity, and Planetary Albedo

A framework is adopted to derive the functional relationships where outgoing radiation under sky condition $i$ (signifying either clear-sky, cloudy-sky, or all-sky conditions, where a cloudy sky is defined to have a cloud amount of 1 if cloud amount varies from 0 to 1) is related to the Stefan-Boltzman constant, $\sigma$ in $\mathrm{Wm^{-2}K^{-4}}$, surface temperature, $T_S$, and incident solar radiation via, $R_{\mathrm{in}}$, in $\mathrm{Wm^{-2}}$, via,

$$R_{\mathrm{out},i}(x,y) = L_{\mathrm{out},i}(x,y) + S_{\mathrm{out},i}(x,y) = \varepsilon_i(x,y)\sigma T_S^4(x,y) + \alpha_i(x,y)\,R_{\mathrm{in}}(x,y) \tag{3}$$

where the planetary emissivity $\varepsilon_i$ is defined by the outgoing longwave radiation at TOA as a fraction of the expected emitted radiation at the planet's surface for a black body averaged over some time span,

$$\varepsilon_i(x,y) = \int_t^{t+n\Delta t} \frac{L_{\mathrm{out},i}(x,y,t')}{\sigma T_S^4(x,y,t')} dt' \Big/ \int_t^{t+n\Delta t} dt', \tag{4a}$$

and the planetary albedo $\alpha_i$ in Equation 3 is defined as the outgoing shortwave radiation at TOA as a fraction of incident solar radiation at TOA averaged over some time span,

$$\alpha_i(x,y) = \int_t^{t+n\Delta t} \frac{S_{\mathrm{out},i}(x,y,t')}{R_{\mathrm{in}}(x,y,t')} dt' \Big/ \int_t^{t+n\Delta t} dt' \,. \tag{4b}$$

#### 2.1.1. Planetary Emissivity

The definition of planetary emissivity adopted here, $\varepsilon_i$ in Equation 4a, considers outgoing radiation measured at TOA and emitted radiation measured at the planet's surface. This planetary emissivity therefore accounts for both the direct emissivity effect of the surface material of the planet (where emitted radiation is less than $\sigma T_S^4$) and the greenhouse effect of the atmosphere (where the atmosphere both absorbs and re-emits longwave radiation so that the outgoing longwave radiation at TOA is less than the upward longwave radiation at the planet's surface). Note that the Sherwood et al. (2020) climate feedback review also utilizes the same planetary emissivity definition when analyzing the Planck feedback.

The climatological monthly mean clear sky planetary emissivity, $\varepsilon_{\mathrm{ClearSky}}(x,y)$, for the period 2003–2023 varies spatially from 0.57 to 1.0 (Figure 2, left hand column), with low values in tropical regions and high values near the poles. This range of values implies that atmospheric absorption and emission of radiation and surface emissivity properties reduce TOA outgoing longwave radiation, relative to the expected longwave blackbody radiation emitted by the Earth's surface, by up to 43% under clear skies. In all sky conditions, monthly mean planetary emissivity, $\varepsilon_{\mathrm{AllSky}}$, varies spatially from 0.39 to 1.0, such that in the presence of clouds outgoing longwave radiation at TOA is reduced by up to 61% relative to the expected surface emission by a blackbody.

#### 2.1.2. Planetary Albedo

The definition of planetary albedo definition adopted here, $\alpha_i$ in Equation 4b, considers incident and reflected radiation both measured at TOA. This planetary albedo definition therefore accounts for the shortwave radiation reflection both by the planet's surface and by atmospheric constituents in either clear sky, cloudy sky or all sky conditions. The monthly climatological planetary albedo varies spatially from <0.10 to 0.88 in clear sky conditions and 0.10 to 0.96 in all sky conditions (Figure 3).

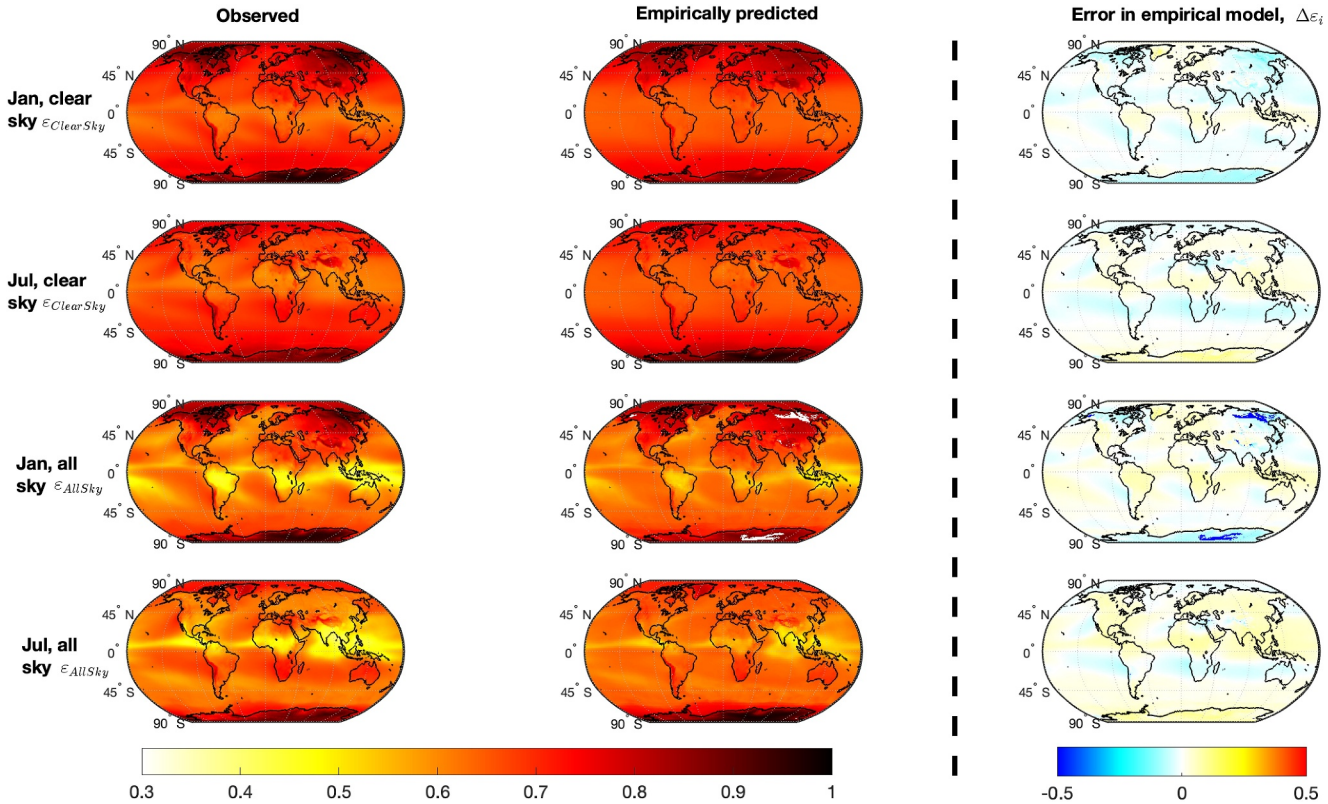



**Figure 2.** Monthly climatological planetary emissivity for 2003–2023 from observations (left hand column), a reduced physics simplified empirical relation (middle column) and the error in the empirical relation (right hand column). Shown are planetary emissivity in clear sky conditions (top two rows) and all sky conditions (bottom two rows) for the months of January and July.

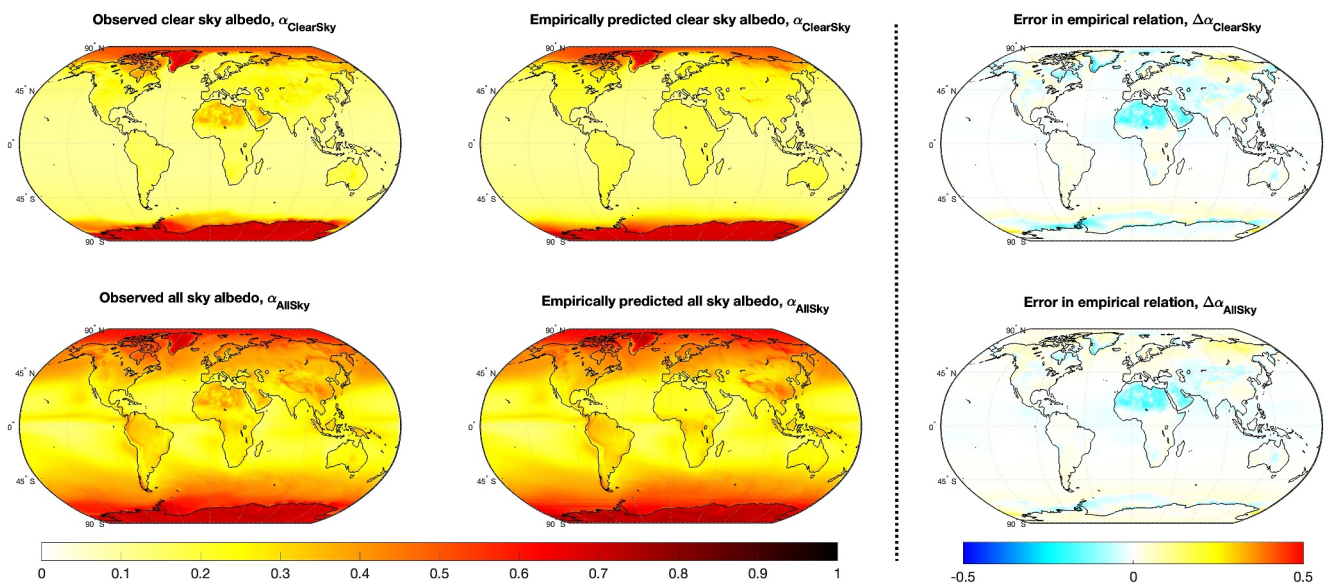



**Figure 3.** Annual climatological albedo in all sky and clear sky conditions from observations (left hand column), from the empirically constrained predictions (middle column) and the error in the empirical predictions (right hand column). The rms error in the empirical relation for planetary albedo is 0.037 for clear sky and 0.030 for all sky conditions.



21698996, 2025, 12, Downloaded from https://agupubs.onlinelibrary.wiley.com/doi/10.1029/2024JD043186 by Imperial College London, Wiley Online Library on [19/10/2026]. See the Terms and Conditions (https://onlinelibrary.wiley.com/terms-and-conditions) on Wiley Online Library for rules of use; OA articles are governed by the applicable Creative Commons License

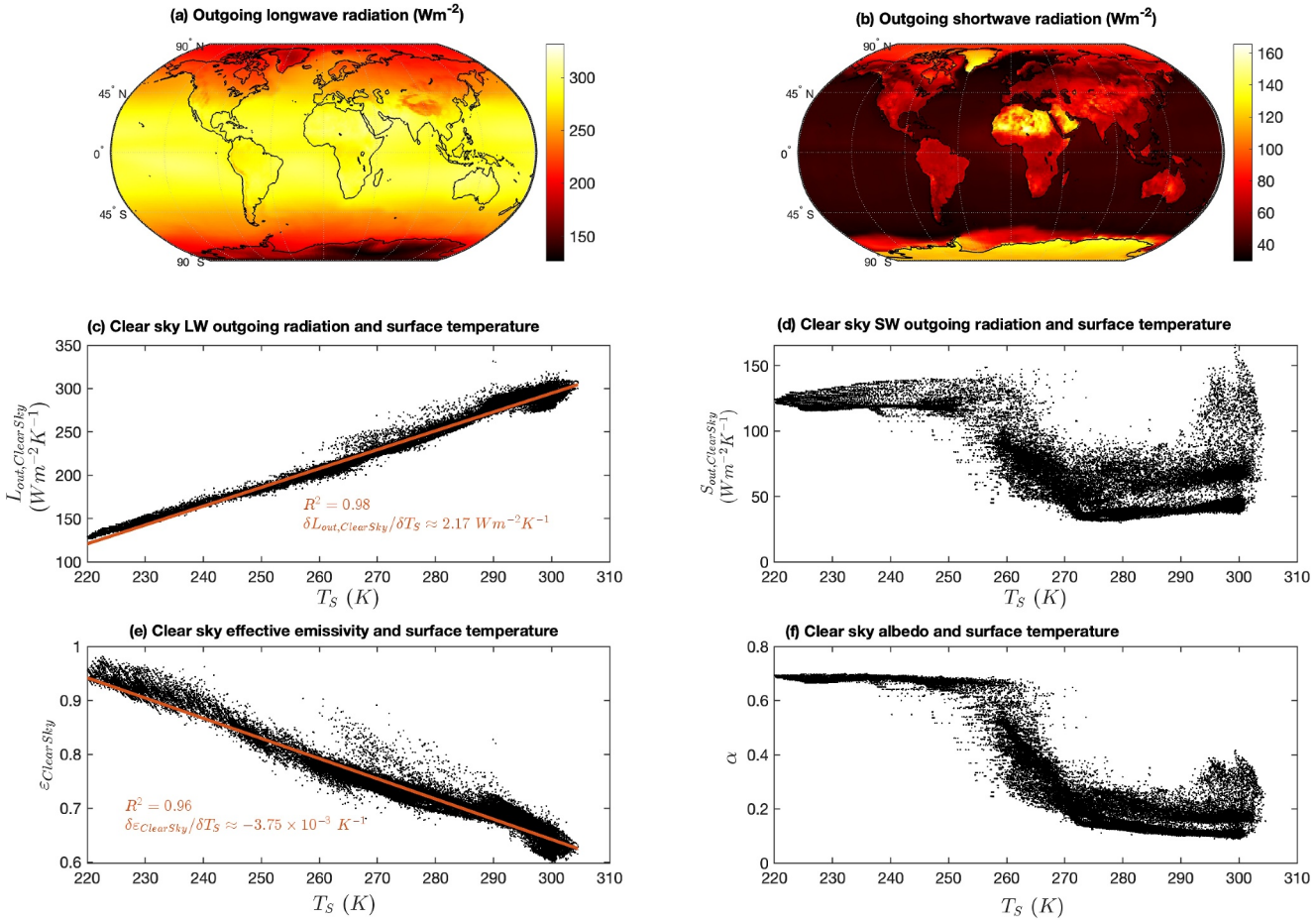



**Figure 4.** Spatial variation in outgoing radiation, planetary emissivity, and albedo for the period 2003–2023 in clear sky conditions, analyzed as annual-mean climatology for 1° by 1° horizontal resolution. (a) Outgoing longwave radiation in clear sky conditions. (b) Outgoing shortwave radiation in clear sky conditions. (c) Outgoing longwave radiation in clear sky conditions and surface temperature. (d) Outgoing shortwave radiation in clear sky conditions and surface temperature. (e) Planetary emissivity in clear sky conditions and surface temperature. (f) Planetary albedo in clear sky conditions and surface temperature.

### 2.1.3. Differential Forms for Planetary Emissivity and Planetary Albedo

From Equation 3 we can see that the TOA outgoing shortwave radiation is related to incoming solar radiation by $S_{\text{out},i}(x,y) = \alpha_i(x,y)R_{\text{in}}(x,y)$ and the TOA outgoing longwave radiation is related to the expected blackbody emission at the Earth's surface by $L_{\text{out},i}(x,y) = \varepsilon_i(x,y)\sigma T_S^4(x,y)$ under sky condition $i$. The values of planetary albedo and planetary emissivity vary spatially (Figures 2 and 3) and with surface temperature (Figure 4). The goal is therefore to identify reduced physics simplified relations for $\alpha_i$ and $\varepsilon_i$ that are differentiable with respect to surface temperature to identify the Planck, WVLR and fixed-cloud albedo climate feedbacks in clear sky and all sky conditions.

In order to be differentiable with respect to surface temperature to evaluate the climate feedback, the simplified relations that solve for TOA outgoing shortwave and longwave radiation, via solving for $\alpha_i$ and $\varepsilon_i$, must only contain parameters that are relatively insensitive to perturbations in surface temperature. Consider two simplified functions where planetary emissivity is related to surface temperature and $J$ other parameters describing the atmospheric and surface properties,

$$\varepsilon_i = f(T_S, x_1, x_2 \ldots x_J) \tag{5a}$$

and planetary albedo is related to surface temperature and $K$ other properties,



21698996, 2025, 12, Downloaded from https://agupubs.onlinelibrary.wiley.com/doi/10.1029/2024JD043186 by Imperial College London, Wiley Online Library on [19/10/2026]. See the Terms and Conditions (https://onlinelibrary.wiley.com/terms-and-conditions) on Wiley Online Library for rules of use; OA articles are governed by the applicable Creative Commons License

$$\alpha_i = g(T_S, y_1, y_2 \ldots y_K) \tag{5b}$$

Ideally, we should like all other parameters to be orthogonal to $T_S$ under climate perturbation so that so that we are to differentiate these functions, $f$ and $g$, with respect to surface temperature without knowing the sensitivity of each separate parameter to $T_S$, $\frac{\partial x_j}{\partial T_S}$. Given that we may not be able to identify parameters that are perfectly orthogonal to $T_S$ and still accurately capture the variation in $\varepsilon_i$ and $\alpha_i$, then we require:

$$\left|\frac{\partial \varepsilon_i}{\partial T_S}\right| \gg \left|\frac{\partial x_j}{\partial T_S}\frac{\partial \varepsilon_i}{\partial x_j}\right| \tag{6a}$$

for each of the $J$ parameters that are not $T_S$ in the emissivity relation Equation 5a and

$$\left|\frac{\partial \alpha_i}{\partial T_S}\right| \gg \left|\frac{\partial y_k}{\partial T_S}\frac{\partial \alpha_i}{\partial y_k}\right| \tag{6b}$$

for each of the $K$ parameters that are not $T_S$ in the albedo relation Equation 5b. Therefore, here we cannot use parameters such as total precipitable column water vapor or specific humidity, since these parameters vary significantly over time with a surface temperature perturbation. For example, if $x_j$ were precipitable water vapor column then after temperature increase $x_j$ would also increase, $\frac{\partial x_j}{\partial T_S} > 0$, since warm air holds more water vapor. This increase in precipitable water vapor column then reduces planetary emissivity, $\frac{\partial \varepsilon_i}{\partial x_j} < 0$, from the greenhouse effect. Therefore the magnitude $\left|\frac{\partial x_j}{\partial T_S}\frac{\partial \varepsilon_i}{\partial x_j}\right|$ could be considerable, and break condition Equation 6a. However, instead we can use parameters such as surface relative humidity and the height of the tropopause (that are related to specific humidity and total precipitable water vapor content), since the changes in these quantities over time after temperature perturbation have a greater chance of satisfying condition Equations 6a and 6b. For example, if $x_j$ were relative humidity then $x_j$ would not likely change significantly with surface warming, $\frac{\partial x_j}{\partial T_S} \sim 0$, and so $\left|\frac{\partial x_j}{\partial T_S}\frac{\partial \varepsilon_i}{\partial x_j}\right|$ would satisfy condition Equation 6a.

### 2.1.4. Clear Sky, Cloudy Sky, and All Sky Conditions

In clear sky conditions, the 2003–2023 annual-mean climatology evaluated planetary emissivity, $\varepsilon_{\text{ClearSky}}$, is nearly linearly related to surface temperature (Figure 4e): $\frac{\delta \varepsilon_{\text{ClearSky}}}{\delta T_S} = -3.75\ \text{K}^{-1}$ with $R^2$ of 0.96 (see Koll and Cronin, 2018). The 2003–2023 annual-mean climatology evaluated clear sky planetary albedo, $\alpha_{\text{ClearSky}}$ (Figure 4f), shows a non-linear relationship to surface temperature with generally high albedo for annual-mean temperatures below 260 K (cold enough for the cryosphere to persist much of the year) and generally low albedo for annual-mean temperatures above 270 K (too warm for the cryosphere). Some locations with temperatures above 290 K show increased albedo, reflecting hot dry dessert regions over land with low plant coverage. Since climate feedbacks are related to the partial derivative of outgoing radiation with respect to surface temperature (Equations 1 and 2), this study aims to identify the partial derivatives, $\frac{\partial \varepsilon_{\text{ClearSky}}}{\partial T_S}$, $\frac{\partial \varepsilon_{\text{AllSky}}}{\partial T_S}$, $\frac{\partial \alpha_{\text{ClearSky}}}{\partial T_S}$ and $\frac{\partial \alpha_{\text{AllSky}}}{\partial T_S}$ through observation-constrained functional relationships that are used to extract the impact of any factors that co-vary spatially with surface temperature in recent climatology (Figure 4). The values of $\frac{\partial \alpha_{\text{ClearSky}}}{\partial T_S}$ and $\frac{\partial \alpha_{\text{AllSky}}}{\partial T_S}$ will necessarily come from non-linear functions that approximate the nonlinear relation between $\alpha_{\text{ClearSky}}$ and $T_S$ (Figure 4f).

The planetary emissivity and albedo for the three different sky conditions, all sky, clear sky, and cloudy sky, are connected via,

$$\varepsilon_{\text{AllSky}}(x,y) = f_{\text{CA}}(x,y)\varepsilon_{\text{CloudySky}}(x,y) + \left[1 - f_{\text{CA}}(x,y)\right]\varepsilon_{\text{ClearSky}}(x,y) \tag{7a}$$

and

$$\alpha_{\text{AllSky}}(x,y) = f_{\text{CI}}(x,y)\alpha_{\text{CloudySky}}(x,y) + \left[1 - f_{\text{CI}}(x,y)\right]\alpha_{\text{ClearSky}}(x,y) \tag{7b}$$

where $f_{\text{CA}}$ is the cloud amount area fraction and $f_{\text{CI}}$ is the cloud incident radiation fraction. Note that when averaging over time the cloud incident radiation fraction may differ from the cloud amount area fraction, and is calculated via



21698996, 2025, 12, Downloaded from https://agupubs.onlinelibrary.wiley.com/doi/10.1029/2024JD043186 by Imperial College London, Wiley Online Library on [19/10/2026]. See the Terms and Conditions (https://onlinelibrary.wiley.com/terms-and-conditions) on Wiley Online Library for rules of use; OA articles are governed by the applicable Creative Commons License

$$f_{\mathrm{CI}}(x,y) = \frac{\sum f_{\mathrm{CA}}(x,y,m)\, R_{\mathrm{in}}(x,y,m)\Delta t_m}{\sum R_{\mathrm{in}}(x,y,m)\Delta t_m} \tag{8}$$

where $m$ is some time interval.

Section 2.1 considers the planetary emissivity and albedo in clear sky conditions, whereas Section 2.2 explores the impact of clouds in modifying the planetary emissivity and albedo in all sky conditions.

## 2.2. TOA Outgoing Radiation in Clear Skies

### 2.2.1. Outgoing Shortwave Radiation for Clear Sky

Simplified functional relationships are now assessed for clear sky planetary albedo, $\alpha_{\mathrm{ClearSky}}$, in terms of surface temperature and other properties of the climate system. Here, we allow clear sky planetary albedo to be a function of surface temperature $T_s$, whether the surface is land or ocean, $k$, and latitude $\phi$,

$$\alpha_{\mathrm{ClearSky}} \approx f(T_s, k, \phi) \tag{9}$$

where the explicit latitudinal dependency on $\phi$ is assumed to arise solely due to the geometrical effect of changes in mean annual solar zenith angle. The temperature effect on $\alpha_{\mathrm{ClearSky}}$ in Equation 9 is assumed to implicitly represent both changes to the surface albedo through the cryosphere and changes to clear sky albedo from changing clear sky atmospheric properties, for example, changes in the amount of water vapor altering the absorption and scattering of shortwave radiation (e.g., Pincus et al., 2015). The impacts of this implicit simplification on the results are discussed below. Observations reveal how monthly climatology $\alpha_{\mathrm{ClearSky}}$ varied seasonally and spatially during the period 2003–2023 (Figure 3), with generally high values for high-latitude snow and ice covered regions and lower values over sea and vegetation-covered land regions. The annual-mean values of local clear sky planetary albedo for the 2003–2023 climatology, $\alpha_{\mathrm{ClearSky}}$, reflect differences due to annual mean surface temperature, latitude and whether the local region is land or sea (Figure 5a, gray and green). The monthly mean albedo values are converted to annual means using insolation-weighting, so at high latitudes the summer months contribute more to the annual mean, in line with the mean solar-zenith angle arguments of Cronin (2014).

Now consider the functional forms for annual-mean albedo at some specified spatial coordinates in terms of latitude and surface temperature over land and ocean, Equation 9. First, we seek to explore the latitudinal dependence, $\phi$, and then later the temperature dependence, $T_s$, for land and ocean, $k$. The latitudinal dependence of albedo is assumed to arise due to the change in solar zenith angle affecting the amount of incident light reflected at any given time, and across a year. The annual-mean planetary albedo for surface-type $j$ at latitude $\phi$, $\alpha_j(\phi)$, is assumed to be related to the planetary-mean albedo for a planet covered entirely by the same surface-type $j$, $\overline{\alpha_j}$, via a relation containing a second order Legendre polynomial in $\sin\phi$ after Goodwin and Williams (2023), with an additional coefficient added here, $\beta$, giving,

$$\alpha_j(\phi) = \left[1 + [1 - \overline{\alpha_j}]\beta\left[\frac{1}{2}[3\,\sin^2\phi - 1]\right]\right]\overline{\alpha_j} \tag{10}$$

The additional coefficient $\beta$ is a tunable parameter within the range $0 \le \beta \le 1$, where 0 indicates no latitudinal dependence on albedo for surface-material $j$ due to latitudinal geometry and 1 indicates the maximum possible latitudinal dependence. Note that when both constraints $0 \le \beta \le 1$ and $0 \le \overline{\alpha_j} \le 1$, Equation 10 implies physically plausible values for local albedo, $0 \le \alpha_j(\phi) \le 1$, for all $\phi$. The second order Legendre polynomial sine of latitude is able to accurately account for how the annual-mean solar zenith angle by the Earth with latitude (e.g., Hartmann, 1994), providing some confidence for its application (with altered coefficients) to account for how annual-mean solar zenith angle affects albedo with latitude (Goodwin and Williams, 2023).

The annual-mean local albedo is generally higher for cold regions that are covered in snow and ice most or all of the year and have lower water vapor levels, and generally lower for warmer regions that are ice- and snow-free for most of the year and have higher water vapor levels (Figure 5a). Applying Equation 10 to each annual-mean local



21698996, 2025, 12, Downloaded from https://agupubs.onlinelibrary.wiley.com/doi/10.1029/2024JD043186 by Imperial College London, Wiley Online Library on [19/10/2026]. See the Terms and Conditions (https://onlinelibrary.wiley.com/terms-and-conditions) on Wiley Online Library for rules of use; OA articles are governed by the applicable Creative Commons License

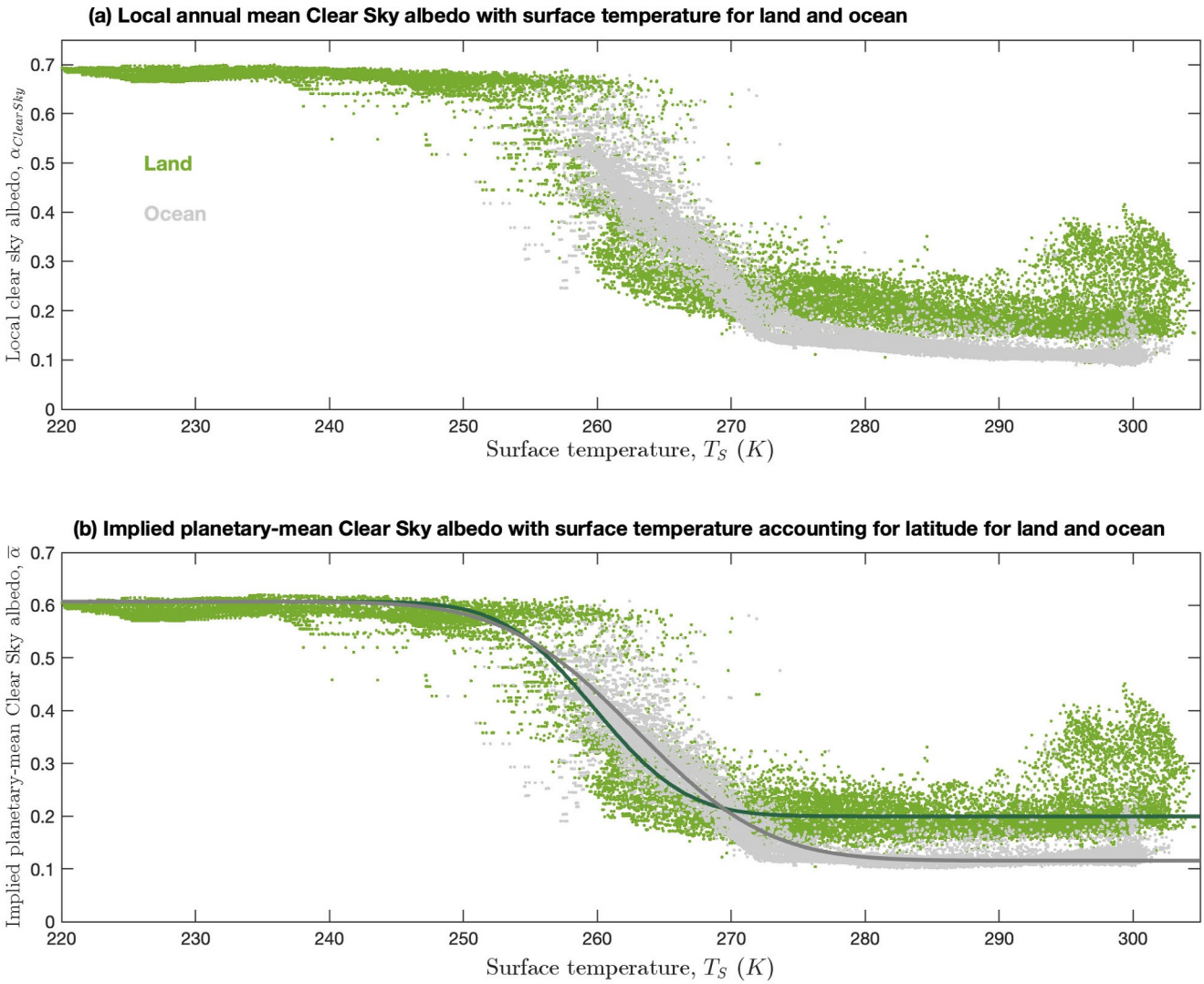



**Figure 5.** Local albedo over land and ocean with surface temperature for the climatological period 2003–2023. (a) The local annual-mean clear sky planetary albedo with surface temperature evaluated over 1° by 1° resolution. (b) The implied global-mean clear sky planetary albedo if the entire planet was covered in the surface-type found at that location, evaluated over 1° by 1° resolution.

albedo value ($\alpha_j$: Figure 3a) would then reveal the effective planetary-mean albedo for a planet entirely covered by the surface material found at that location ($\overline{\alpha_J}$). This approximation is assumed here to effectively strip away the latitudinal impact on local fixed-cloud albedo, and leave only the temperature and land or ocean factors. To do this, we must first identify an approximate functional relationship between temperature and $\overline{\alpha_J}$ for land and ocean that will then be empirically constrained.

How should temperature impact clear sky albedo? Here, we assume that when the ocean is warm enough to be ice-free all year, then increasing the temperature further has no impact on local albedo. Therefore, the reduction in local albedo over the ocean as temperatures warm from 280 to 300 K is assumed here to be a latitudinal geometry effect arising from variation in mean annual solar zenith angle (Figure 5a, gray), consistent with previous observational analysis of sea surface albedo with solar zenith angle (Payne, 1972). Similarly, we assume that when the land is cold enough to be ice-covered all year, reducing the temperature further has no impact on local albedo. Therefore, the increase in local albedo when annual land temperatures reduce from 245 to 220 K (Figure 5a, green) is assumed here to be a latitudinal geometry effect. We seek a functional form that, on an $\overline{\alpha_J}$-$T_S$ plot has a low dependence at high and low temperatures, with high $\overline{\alpha_J}$ at low $T_S$ and low $\overline{\alpha_J}$ at high $T_S$, and has a continuous and differentiable form between these limiting values (e.g., Figure 5b, lines).



21698996, 2025, 12, Downloaded from https://agupubs.onlinelibrary.wiley.com/doi/10.1029/2024JD043186 by Imperial College London, Wiley Online Library on [19/10/2026]. See the Terms and Conditions (https://onlinelibrary.wiley.com/terms-and-conditions) on Wiley Online Library for rules of use; OA articles are governed by the applicable Creative Commons License

21698996, 2025, 12, Downloaded from https://agupubs.onlinelibrary.wiley.com/doi/10.1029/2024JD043186 by Imperial College London, Wiley Online Library on [19/10/2026]. See the Terms and Conditions (https://onlinelibrary.wiley.com/terms-and-conditions) on Wiley Online Library for rules of use; OA articles are governed by the applicable Creative Commons License

The temperature dependence of the planetary albedo for a planet entirely covered by either land or ocean, $\overline{\alpha_{\text{ClearSky},k}}$, is assumed to be represented by a relation containing the error function with respect to annual mean surface temperature via (e.g., Figure 5b, lines)

$$\overline{\alpha_{\text{ClearSky},k}}(T_S) = \left(\frac{\overline{\alpha_{\text{warm},k}} + \overline{\alpha_{\text{cold},k}}}{2}\right) - \left(\frac{\overline{\alpha_{\text{cold},k}} - \overline{\alpha_{\text{warm},k}}}{2}\right) \text{erf}\left(\frac{T_s - (T_{\text{warm},k} + T_{\text{cold},k})/2}{(T_{\text{warm},k} - T_{\text{cold},k})/2}\right) \tag{11}$$

where $k$ indicates either land or ocean, $\overline{\alpha_{\text{warm},k}}$ is the planetary mean albedo covered in surface $k$ held at temperatures with no snow or ice, $\overline{\alpha_{\text{cold},k}}$ is the planetary mean albedo for surface $k$ held at temperatures where there is snow or ice all year, $T_{\text{warm},k}$ is the annual mean temperature above which the surface has very little snow or ice at any time of year, and $T_{\text{cold},k}$ is the annual mean temperature below which the surface is almost entirely snow or ice covered all year.

The latitudinal dependence on clear sky planetary albedo is then modeled using a second order Legendre polynomial (Equation 10) to convert $\overline{\alpha_{\text{ClearSky},k}}$ to $\alpha_{\text{ClearSky}}$,

$$\alpha_{\text{ClearSky}}(x,y,T_S) = \left[1 + \left[1 - \overline{\alpha_{\text{ClearSky}}}(x,y,T_S)\right]\beta\left[\frac{1}{2}\left[3\,\sin^2\phi - 1\right]\right]\right]\overline{\alpha_{\text{ClearSky}}}(x,y,T_S) \tag{12}$$

Closures Equations 10 and 11 have tunable parameters $\beta$, $\overline{\alpha_{\text{warm,land}}}$, $\overline{\alpha_{\text{cold,land}}}$, $\overline{\alpha_{\text{warm,ocean}}}$, $\overline{\alpha_{\text{cold,ocean}}}$, $T_{\text{warm,land}}$, $T_{\text{cold,land}}$, $T_{\text{warm,ocean}}$ and $T_{\text{cold,ocean}}$. These parameters are tuned to minimize the root of mean squares error in how Equations 10 and 11 estimate $\alpha_{\text{ClearSky}}(x,y,T_S)$ from observed climatology (Table S1 in Supporting Information S1; Figure 5b, compare lines to dots). This is achieved in two stages: first the values of the parameters are fitted to $\alpha_{\text{ClearSky}}(x,y,T_S)$ over land for all land points with $T_S < 290$ K (since we are not attempting to include desertification at high temperatures within out scheme, Figure 5a, green). Secondly, the values of the parameters are fitted for the ocean assuming that $\overline{\alpha_{\text{cold},k}}$ and $\beta$ are the same for the ocean as the land (as the lack of data points with very low temperatures above the ocean, Figure 5a, gray, makes $\overline{\alpha_{\text{cold,ocean}}}$ and in turn $\beta$ difficult to fit, and very low temperatures are assumed to be entirely ice or snow covered all year regardless of whether they are over land or ocean).

These relations, Equations 10–12 with the tuned values of $\beta$, $\overline{\alpha_{\text{warm,land}}}$, $\overline{\alpha_{\text{cold,land}}}$, $\overline{\alpha_{\text{warm,ocean}}}$, $\overline{\alpha_{\text{cold,ocean}}}$, $T_{\text{warm,land}}$, $T_{\text{cold,land}}$, $T_{\text{warm,ocean}}$ and $T_{\text{cold,ocean}}$ (Table S1 in Supporting Information S1), predict the clear sky albedo over each $1° \times 1°$ surface location based on the annual mean surface temperature (Figure 5b, compare lines to dots). The statistical models (Equations 10 and 11; Figure 5b, compare lines to dots) have $R^2 = 0.962$ for $\alpha_{\text{ClearSky}}(x,y,T_S)$ over the ocean and $R^2 = 0.949$ over land ($T_S < 290$ K), and predict $\alpha_{\text{ClearSky}}(x,y,T_S)$ values with a root mean square error of 0.0268 over the ocean and 0.0486 over land with $T_S < 290$ K (Figure 3). Note that variation in atmospheric aerosol loading are not considered in the equations, and will lead to scatter between observed and empirically constrained values (Figure 5b). The annual clear sky albedo $\alpha_{\text{ClearSky}}(x,y,T_S)$ ranges from 0.09 to 0.70 and is spatially well predicted from $T_s$, $k$ and $\phi$ by the empirical relations (Equations 9–12; Figure 3, top row) with an overall rms error of 0.04. The largest local errors on land arise in desert and grassland regions, which have higher local clear sky albedo than other land regions at the same temperature, and in the ocean arise at the northernmost edge of the Southern Ocean sea-ice extent, where local clear sky albedo is slightly underestimated in the empirical predictions (Figure 3).

The functions adopted here to describe the latitudinal and temperature impacts on clear sky albedo (Equations 10 and 11) are reasonable since:

1. The single fitted value of $\beta = 0.33 \pm 0.01$ produces the correct equatorial to high-latitude variation in *clear sky* albedo over the ocean (Figure 3, top row, consider regions warm enough to remove any significant sea ice) and the correct equatorial to high-latitude variation in *sea surface* albedo in the Atlantic Ocean analyzed by Payne (1972) (see Text S3 in Supporting Information S1: Payne (1972) observes annual equatorial sea surface albedo of 0.06 increasing to between 0.08 and 0.10 for +60° to +70° latitude, in line with Equation 10 using $\beta = 0.33$ and $\overline{\alpha_J}$ tuned to give equatorial albedo of 0.06). This agreement indicates that the latitudinal variation observed is explainable primarily due to a solar zenith angle geometry affecting the planetary surface

21698996, 2025, 12, Downloaded from https://agupubs.onlinelibrary.wiley.com/doi/10.1029/2024JD043186 by Imperial College London, Wiley Online Library on [19/10/2026]. See the Terms and Conditions (https://onlinelibrary.wiley.com/terms-and-conditions) on Wiley Online Library for rules of use; OA articles are governed by the applicable Creative Commons License

reflection as assumed in the equations, and not a latitudinal variation in atmospheric absorption since this does not affect *sea surface* albedo;

2. The single fitted value of $\beta = 0.33 \pm 0.01$ removes any significant slope in planetary clear sky albedo with temperature at both warm locations, for ocean and land, and cold locations, over land (compare Figures 5b–5a, green and gray dots), showing that the latitudinal geometry impact on local clear sky albedo is accurately accounted for across different surface types; and
3. The fitted parameter values (Table S1 in Supporting Information S1) are able to accurately calculate the planetary albedo calculated for each location with low rms error (Figure 5b compare lines to dots), showing that the surface temperature impact on albedo is accurately accounted for.

There is more error in the land reconstruction than for the ocean, in part since the land has very warm regions that are dry and so have low vegetation and high albedo (Figure 5). The functional equations chosen are only intended to account for the cryosphere impact on albedo with temperature, not the impact from the drying out of soils and changing of the vegetation state.

The annual mean clear sky albedo $\alpha_{\text{ClearSky}}$ ranges from 0.09 to 0.70 (Figure 5a), whereas the implied global annual mean clear sky albedo if the entire planet was covered in that surface material $\overline{\alpha_{\text{ClearSky}}}$ ranges from 0.10 to 0.66 (Figure 5b). The range in $\alpha_{\text{ClearSky}}$ is due to both surface temperature (via the cryosphere extent and atmospheric water vapor) and solar zenith angle, whereas $\overline{\alpha_{\text{ClearSky}}}$ has the solar zenith angle effect removed. The reduced range in $\overline{\alpha_{\text{ClearSky}}}$ compared to $\alpha_{\text{ClearSky}}$ implies that some 91% of the observed range in clear sky albedo is functionally related to surface temperature, whereas 9% is due to variation in factors that co-vary with temperature in space but would not co-vary with surface temperature in time following perturbation, such as the solar zenith angle change with latitude.

### 2.2.2. Outgoing Longwave Radiation for Clear Sky

Simplified functional relationships are now assessed for clear sky planetary emissivity in terms of surface temperature and other climate properties. Based on simple physical considerations, we expect that clear sky planetary emissivity, $\varepsilon_{\text{ClearSky}}$, will decrease with:

- an increase in surface temperature $T_S$, since warmer air holds more water vapor;
- an increase in mid-troposphere relative humidity $H_{\text{rel}}$, since water vapor is a greenhouse gas (see Feng et al. (2023b) for discussion of why outgoing longwave radiation is best related to the average *mid-troposphere* relative humidity from 250 to 750 hPa);
- an increase in the height of the tropopause above the surface, $z_{\text{trop}} - z_s$, since a higher tropopause indicates that water vapor extends to a greater height in the atmosphere and reflects changes to the lapse rate;
- an increase in surface pressure, $p_s$, since this indicates a greater mass of atmosphere above the surface, and so greater greenhouse effect.

Based on these physical considerations, we postulate a simplified linearized relationship whereby planetary emissivity is linearly related to surface temperature, $T_S$; relative humidity in the mid-troposphere (250–750 hPa: Feng et al., 2023b), $H_{\text{rel}}$; the height of the tropopause above local surface elevation, $z_{\text{trop}}(x,y,t) - z_s(x,y)$; and surface pressure, $p_s$, via,

$$\varepsilon_{\text{ClearSky}}(x,y,t) \approx c_o + c_1 T_S(x,y,t) + c_2 H_{\text{rel}}(x,y,t) + c_3 [z_{\text{trop}}(x,y,t) - z_s(x,y)] + c_4\, p_s(x,y,t) \tag{13}$$

For monthly mean observed climatology from 2003 to 2023 on a 1° by 1° spatial resolution, the coefficients for Equation 13 are fitted (Table S2 in Supporting Information S1). The empirically constrained simplified relation calculates $\varepsilon_{\text{ClearSky}}(x,y,t)$ across all 12 months and each 1° by 1° location with a root of mean squares error of 0.0248, and has an adjusted $R^2$ value of 0.906, thus providing accurate monthly spatial estimates of planetary clear sky emissivity (Figure 2, top two rows). In addition to producing predictions in agreement with observations (Figure 2), if the simple physical justification for Equation 13 holds then we should also expect that the empirically fitted coefficient values $c_1$, $c_2$, $c_3$ and $c_4$ should all be negative, which they are (Table S2 in Supporting Information S1). Note that additional processes may affect how vertical temperature structure and outgoing longwave radiation change over time but are not considered in this methodology (i.e., a lapse rate component of the feedback that is not linked to changes in tropopause height). Such processes would alter

$\varepsilon_{\text{ClearSky}}(x,y,t)$ over time in a way that is not captured by Equation 13. The applicability of Equation 13 for spatial variation is supported by results from Feng et al. (2023a), who find that the vertical temperature structure (lapse rate) is not of primary importance in varying outgoing longwave radiation spatially.

The coefficient $c_1$ takes the value $c_1 = \frac{\partial \varepsilon_{\text{ClearSky}}}{\partial T_S} = -(-2.904 \pm 0.003) \times 10^{-3}\ \text{K}^{-1}$ when (13) is empirically fitted to data on a monthly climatological basis (Table S2 in Supporting Information S1), indicating that 77% of the observed spatial variation in $\varepsilon_{\text{ClearSky}}$ with $T_S$ ($\frac{\delta \varepsilon_{\text{ClearSky}}}{\delta T_S} = -3.75 \times 10^{-3}\ \text{K}^{-1}$: Figure 4e) is functionally due to variation in surface temperature, whereas 23% of the observed variation is due to variation in factors that co-vary with temperature in space but would not co-vary with surface temperature in time following perturbation. For example, spatial locations with high surface elevation and low surface pressure are generally also cold and have high planetary emissivity, $\varepsilon_{\text{ClearSky}}$. There is also a near-linear relationship between $L_{\text{out}}$ and $T_S$ in the region of parameter space considered (Figures 2c and 2e), implying that up to around 77% of the spatial variation in outgoing longwave radiation at TOA is functionally related to surface temperature. See also Feng et al. (2023b) for explanation of the reasons behind outgoing longwave radiation's near linear temperature dependence and its non-linear component.

### 2.3. TOA Outgoing Radiation in All Sky Conditions

#### 2.3.1. Outgoing Shortwave for All Sky

Now, the impact of clouds on the planetary albedo is assessed to constrain a relation for albedo feedback under all sky conditions. The albedo of clouds is evaluated using a model of how clouds either reflect or emit radiation, and the surface of the planet reflects radiation, leading to an infinite series of emission and reflection contributions (Text S1 and Figure S1 in Supporting Information S1). A key difference relative to previous infinite series models (e.g., Taylor et al., 2007) is that here a distinction is made between the albedo of cloud for *directed* incident solar radiation (which is assumed to be latitudinally dependent due to changes in mean solar zenith angle) and the albedo of cloud for *diffuse* upwards radiation that has been reflected by the Earth's surface (which is assumed to be latitudinally independent). This difference in albedo between directed and diffuse light arises because the angle of incidence affects the albedo (e.g., Stephens, 1978).

Adopting this separation of directed and diffuse albedo model (Text S1 and Figure S1 in Supporting Information S1), the cloudy sky albedo is related to the clear sky albedo via,

$$\alpha_{\text{CloudySky}}(x,y) \approx \alpha_{\text{Cloud:dir}}(x,y) + \overline{\alpha_{\text{ClearSky}}}(x,y)\,\frac{\left[1-\alpha_{\text{Cloud:dir}}(x,y)\right]\left[1-\overline{\alpha_{\text{Cloud}}}\right]}{\left[1-\overline{\alpha_{\text{ClearSky}}}(x,y)\times\overline{\alpha_{\text{Cloud}}}\right]} \tag{14}$$

where $\alpha_{\text{Cloud:dir}}(x,y)$ is the annual mean albedo of cloud at location $x,y$ for directed incident solar radiation, $\overline{\alpha_{\text{Cloud}}}$ is the global mean cloud albedo, which is assumed equal to the albedo of cloud for diffuse radiation from below and is invariant with latitude. Using observational estimates for $\alpha_{\text{CloudySky}}(x,y)$ (Figure 3) and modifying observed $\alpha_{\text{ClearSky}}(x,y)$ with Equation 12 to obtain $\overline{\alpha_{\text{ClearSky}}}(x,y)$, Equation 14 is iteratively solved to calculate the climatological spatial pattern of cloud albedo for directed solar radiation, $\alpha_{\text{Cloud:dir}}(x,y)$, for the period 2003–2023 (Figure 6, left hand column), noting that $\overline{\alpha_{\text{Cloud}}}$ is the global average cloud albedo.

The local variations in reconstructed cloud albedo, $\alpha_{\text{Cloud:dir}}$, reflect differences in cloud properties (Figure 6). However, within this variation due to local cloud properties, the evaluated values of $\alpha_{\text{Cloud:dir}}(x,y)$ show a general pattern of increasing with latitude $\phi$ (Figure 6, right hand side), consistent with the Stephens (1978) theoretical model and parameterization identifying how the magnitude of cloud albedo varies with solar zenith angle (see Stephens, 1978, Figure 4 therein).

#### 2.3.2. Outgoing Longwave for All Sky

Now, the impact of clouds on the relationship between clear sky planetary emissivity and surface temperature is considered. Clear sky planetary emissivity $\varepsilon_{\text{ClearSky}}$ is empirically related to surface temperature via Equation 13. However, to calculate longwave climate feedbacks in all sky conditions, we need to relate planetary emissivity in all sky conditions, $\varepsilon_{\text{AllSky}}$, to $\varepsilon_{\text{ClearSky}}$.



21698996, 2025, 12, Downloaded from https://agupubs.onlinelibrary.wiley.com/doi/10.1029/2024JD043186 by Imperial College London, Wiley Online Library on [19/10/2026]. See the Terms and Conditions (https://onlinelibrary.wiley.com/terms-and-conditions) on Wiley Online Library for rules of use; OA articles are governed by the applicable Creative Commons License

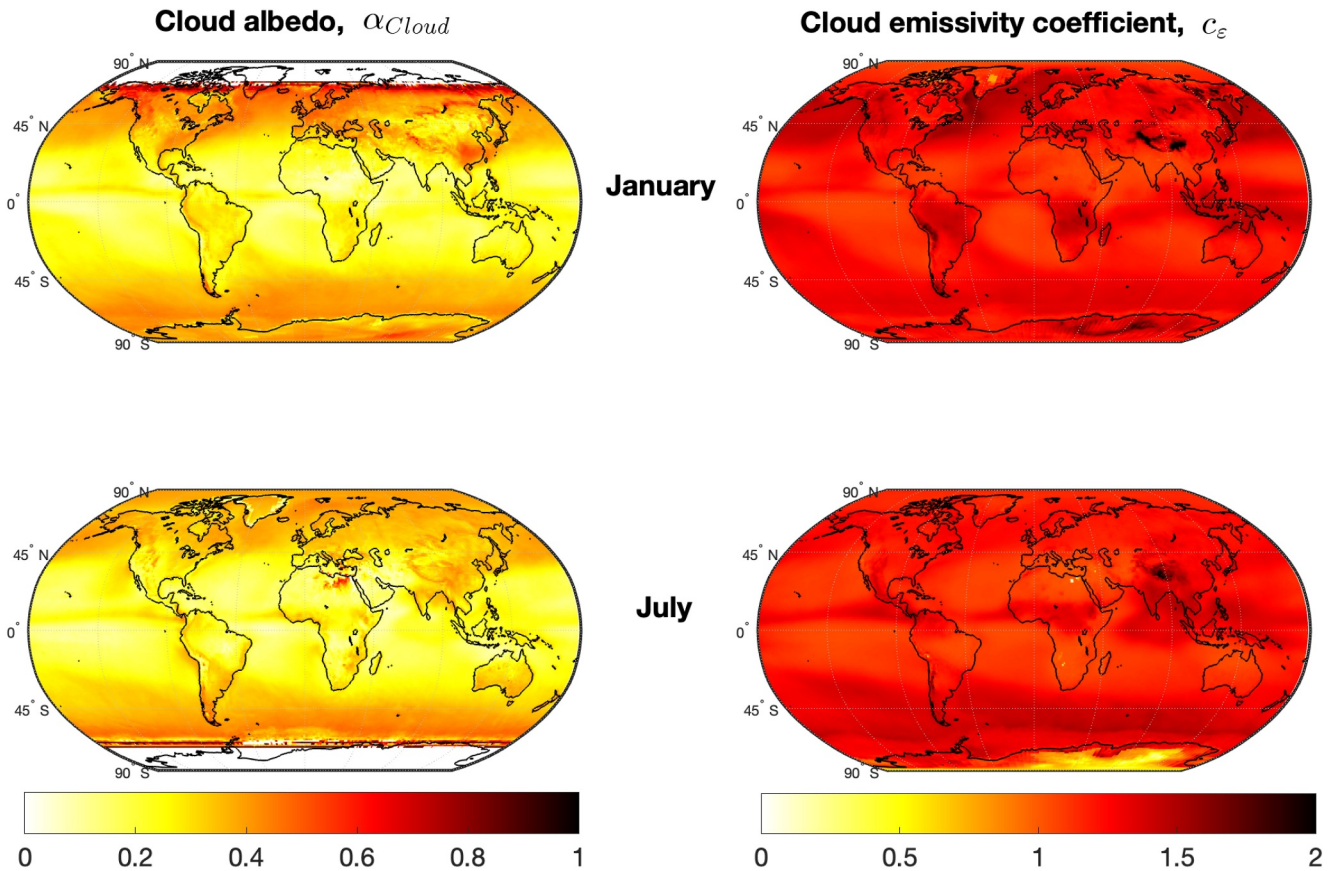



**Figure 6.** The albedo of cloud for directed incident solar radiation (left hand panels) and the cloud emissivity coefficient for outgoing longwave radiation (right hand panels) and the albedo of cloud from monthly mean climatology for 2003–2023.

With no atmosphere, and a perfect blackbody surface, the planetary emissivity would be equal to 1. In clear sky conditions planetary emissivity is less than 1 because greenhouse gasses in the atmosphere reduce the TOA outgoing longwave radiation compared to the expected emission from the surface (Figure 2, left hand column): the ambient reduction in planetary emissivity in clear sky conditions is $1 - \varepsilon_{\text{ClearSky}}$. This ambient planetary emissivity is reduced further in the presence of clouds because clouds themselves reduce TOA outgoing radiation (Figure 2, compare middle and left hand columns): the total reduction in planetary emissivity with clouds and an atmosphere is $1 - \varepsilon_{\text{CloudySky}}$ (Figure S2 in Supporting Information S1).

Since clouds reduce outgoing longwave radiation at the TOA, a recent study (Goodwin and Williams, 2023) expressed this reduction of planetary emissivity due to clouds of clouds via a cloud-emissivity coefficient, $c_\varepsilon = [1 - \varepsilon_{\text{CloudySky}}]/[1 - \varepsilon_{\text{ClearSky}}]$, where $c_\varepsilon$ is an amplification factor by which the value of one minus the emissivity for clear sky conditions is amplified in cloudy sky conditions. The value of $c_\varepsilon$ represents the impact of clouds on the longwave radiation budget and varies with cloud type.

Here, we utilize this cloud-emissivity coefficient to relate $\varepsilon_{\text{AllSky}}$ to $\varepsilon_{\text{ClearSky}}$ and parameters representing cloud amount, $f_{\text{CA}}$, and cloud type, $c_\varepsilon$, of the form

$$\varepsilon_{\text{AllSky}} = \varepsilon_{\text{ClearSky}} - f_{\text{CA}}(c_\varepsilon - 1)(1 - \varepsilon_{\text{ClearSky}}) \quad (15)$$

where the cloud-emissivity coefficient (Goodwin and Williams, 2023) expresses the longwave radiation budget impact of clouds via,



21698996, 2025, 12, Downloaded from https://agupubs.onlinelibrary.wiley.com/doi/10.1029/2024JD043186 by Imperial College London, Wiley Online Library on [19/10/2026]. See the Terms and Conditions (https://onlinelibrary.wiley.com/terms-and-conditions) on Wiley Online Library for rules of use; OA articles are governed by the applicable Creative Commons License

$$c_\varepsilon(x,y,t) = \frac{[1-\varepsilon_{\text{CloudySky}}(x,y,t)]}{[1-\varepsilon_{\text{ClearSky}}(x,y,t)]} \tag{16}$$

Here, the cloud emissivity coefficient of Goodwin and Williams (2023), is re-analyzed for the 2003–2023 period, using monthly climatology at 1° by 1° spatial resolution (Figure 6, right hand panels). The resulting values of $c_\varepsilon$ for across each 1° by 1° gridpoint in each month have a median value of $c_\varepsilon = 1.23$, 66% of values between 1.11% and 1.34% and 90% of values between 1.05 and 1.42 (Figure 6, right hand panels). Therefore, the value of $1-\varepsilon_{\text{CloudySky}}$ is larger than $1-\varepsilon_{\text{ClearSky}}$ by between 5% and 42% across spatial and monthly variation for 90% of the time. Note that the variation in $c_\varepsilon$ values arises for local climate states with very different monthly climatologies, with large variation in surface temperatures, relative humidites, surface elevations and other climatological parameters including cloud type.

Combining the empirical prediction for clear sky planetary emissivity ($\varepsilon_{\text{ClearSky}}$; Equation 13; Figure 2) with the observed spatial monthly climatology for the cloud emissivity coefficient ($c_\varepsilon$; Equation 16; Figure 6), and accounting for observed cloud amount using Equation 7a, produces an empirical relation for all sky planetary emissivity, $\varepsilon_{\text{AllSky}}(x,y,t)$ (Equation 15; Figure 2, bottom two rows), where the empirical prediction in Figure 2 uses $\varepsilon_{\text{ClearSky}}$ values predicted from Equation 13 and $f_{\text{CA}}$ and $c_{\text{ep}}$ as observed from monthly climatology. This empirical prediction for spatial and monthly all sky emissivity is in good agreement with the observed values (Figure 2), with an r.m.s. error of 0.03 (Figure 2, bottom two rows). There is significant local error in isolated cold polar locations where $\varepsilon_{\text{ClearSky}}(x,y,t)$ is close to 1, and the denominator of Equation 16 goes to zero.

## 3. Climate Feedbacks

The simplified functional relationships for planetary emissivity and planetary albedo to calculate the Planck, WVLR and albedo climate feedbacks in clear sky and all sky conditions are now utilized. Cloud feedbacks are not considered. From Equations 1, 2 and 7, the local climate feedback for sky-condition $i$ at location $x,y$ is defined as,

$$\lambda_i(x,y) = -\frac{\partial R_{\text{out},i}}{\partial T_S}(x,y) = -\frac{\partial}{\partial T_S}\left[\varepsilon_i(x,y)\sigma T_S^4(x,y) + \alpha_i(x,y)\,R_{\text{in}}(x,y)\right] \tag{17a}$$

which differentiates giving,

$$\lambda_i(x,y) = \underbrace{-4\varepsilon_i(x,y)\sigma T_S^3(x,y)}_{\text{Planck}} \underbrace{-\sigma T_S^4(x,y)\frac{\partial \varepsilon_i}{\partial T_S}(x,y)}_{\text{WVLR+LWcloud}} \underbrace{-R_{\text{in}}(x,y)\frac{\partial \alpha_i}{\partial T_S}(x,y)}_{\text{albedo+SWCloud}} \tag{17b}$$

To remove the cloud feedbacks from Equations 17a and 17b we set in this study the partial derivatives of emissivity and albedo with surface temperature to be evaluated without a temporal change in cloud amount, cloud emissivity coefficient or cloud albedo, such that $\frac{\partial \varepsilon_i}{\partial T_S} = \left.\frac{\partial \varepsilon_i}{\partial T_S}\right|_{\delta f_{\text{CA}}=\delta c_\varepsilon=\delta\alpha_{\text{Cloud}}=0}$ and $\frac{\partial \alpha_i}{\partial T_S} = \left.\frac{\partial \alpha_i}{\partial T_S}\right|_{\delta f_{\text{CA}}=\delta c_\varepsilon=\delta\alpha_{\text{Cloud}}=0}$. The consequences of changes in cloud amount and cloud properties (via cloud emissivity coefficient and cloud albedo) with time are reserved for future study.

Analyzing the global mean climate feedback for some process and cloud state $\overline{\lambda_i}$ then requires convoluting this spatial feedback Equations 17a and 17b with a warming pattern,

$$\overline{\lambda_i} = \frac{\int \lambda_i(x,y)\Delta T_S(x,y)\,dxdy}{\int \Delta T_S(x,y)\,dxdy} \tag{18}$$

Here, we use the multi-model warming pattern for a 2°C global-mean warming from Assessment Report 6 of the Intergovernmental Panel on Climate Change (IPCC, 2021). The associated 4°C warming pattern (IPCC, 2021) is also used to assess how climate feedbacks vary with the background climate state, by re-analyzing the climate feedback for surface temperature profiles of +2 K and +4 K warming (calculated as the ERA5 temperature profile for 1940–1960 with the +2 K and +4 K IPCC (2021) warming patterns).



21698996, 2025, 12, Downloaded from https://agupubs.onlinelibrary.wiley.com/doi/10.1029/2024JD043186 by Imperial College London, Wiley Online Library on [19/10/2026]. See the Terms and Conditions (https://onlinelibrary.wiley.com/terms-and-conditions) on Wiley Online Library for rules of use; OA articles are governed by the applicable Creative Commons License

21698996, 2025, 12, Downloaded from https://agupubs.onlinelibrary.wiley.com/doi/10.1029/2024JD043186 by Imperial College London, Wiley Online Library on [19/10/2026]. See the Terms and Conditions (https://onlinelibrary.wiley.com/terms-and-conditions) on Wiley Online Library for rules of use; OA articles are governed by the applicable Creative Commons License

**Table 1**
*Climate Feedback Terms and Climate Sensitivity Compared to IPCC Assessment and CMIP Models*

| Climate feedback | This study, 2003–2023 *{median, (66% range) [90% range]}* | This study, +2°C warming *{median, (66% range) [90% range]}* | This study, +4°C warming *{median, (66% range) [90% range]}* | AR6 *{median, (66% range) [90% range]}* | Sherwood et al. *{median, (66% range) [90% range]}* | CMIP6, *{mean ± standard deviation}* |
|---|---|---|---|---|---|---|
| Planck, $\lambda_{\text{Planck}}$ ($\text{Wm}^{-2}\text{K}^{-1}$) | −3.30 | −3.38 | −3.52 | −3.22 (−3.1 to −3.3) [−3.0 to −3.4] | −3.20 (−3.16 to −3.24) [−3.13 to −3.27] | −3.28 ± 0.05 |
| Fixed-cloud albedo, $\lambda_{\text{albedo}}$ ($\text{Wm}^{-2}\text{K}^{-1}$) | 0.64 (0.58–0.70) [0.53 to 0.74] | 0.54 (0.49–0.59) [0.44 to 0.63] | 0.35 (0.32–0.38) [0.29 to 0.41] | 0.35 (0.25–0.45) [0.10 to 0.60] | 0.30 (0.15–0.45) [0.05 to 0.55] | 0.45 ± 0.09 |
| WVLR, $\lambda_{\text{WVLR}}$ ($\text{Wm}^{-2}\text{K}^{-1}$) | 1.28 (1.13–1.45) [1.02 to 1.57] | 1.30[a] (1.14–1.47) [1.03 to 1.60] | 1.35[a] (1.17–1.53) [1.05 to 1.67] | 1.30 (1.2–1.4) [1.1 to 1.5] | 1.15 (1.0–1.3) [0.9 to 1.4] | 1.33 ± 0.09 |
| Cloud, $\lambda_{\text{Cloud}}$ ($\text{Wm}^{-2}\text{K}^{-1}$) | – | – | – | 0.42 (0.12–0.72) [−0.10 to 0.94] | 0.45 (0.12–0.78) [−0.09 to 0.99] | 0.42 ± 0.36 |
| Total climate feedback, $\lambda_{\text{total}}$ ($\text{Wm}^{-2}\text{K}^{-1}$) | −0.95[b] (−0.68 to −1.21) [−0.49 to −1.40] −1.18[c] (−0.94 to −1.41) [−0.77 to −1.58] | – | – | −1.16 (−0.78 to −1.54) [−0.51 to −1.81] | −1.30 (−0.86 to −1.74) [−0.58 to −2.02] | −1.00 ± 0.34 |

*Note.* CMIP6 values taken from Zelinka et al. (2020). [a]Inferred values for a linearized system, without strong constraints for the second derivative of planetary emissivity with respect to surface temperature. [b]Combines Planck, WVLR, and albedo feedbacks with Ceppi and Nowack (2021) evaluated range for cloud feedback. [c]Combines with Raghuraman et al. (2023) evaluated range for cloud feedback.

### 3.1. Planck Feedback

The Planck feedback is defined here as the change in outgoing radiation following a change in surface temperature while atmospheric planetary emissivity is held constant (to represent constant atmospheric constituents). The Planck feedback for clear skies is written, from Equation 11,

$$\lambda_{\text{Planck,ClearSky}}(x,y) = -4\epsilon_{\text{ClearSky}}(x,y)\sigma T_S^3(x,y) \tag{19}$$

while the Planck feedback for all sky conditions is,

$$\lambda_{\text{Planck,AllSky}}(x,y) = -4\epsilon_{\text{AllSky}}(x,y)\sigma T_S^3(x,y) \tag{20}$$

Using monthly mean climatology for the period 2003–2023, the Planck feedback is analyzed, giving a global spatial average of $\lambda_{\text{Planck,ClearSky}} = -3.72\ \text{Wm}^{-2}\text{K}^{-1}$ and $\lambda_{\text{Planck,AllSky}} = -3.33\ \text{Wm}^{-2}\text{K}^{-1}$ for uniform surface warming. When convoluted with a multi-model mean pattern for 2°C global warming (IPCC, 2021), the 2003–2023 all sky Planck feedback becomes $\lambda_{\text{Planck,AllSky}} = -3.30\ \text{Wm}^{-2}\text{K}^{-1}$. This Planck feedback analysis is similar to previous methods (e.g., see Sherwood et al., 2020), and correspondingly gives similar results (Table 1).

### 3.2. Clear Sky and Fixed-Cloud All Sky Planetary Albedo Feedback

The clear-sky albedo feedback is written, from Equations 17a and 17b,

$$\lambda_{\text{albedo,ClearSky}}(x,y) = -R_{\text{in}}(x,y)\frac{\partial \alpha_{\text{ClearSky}}}{\partial T_S}(x,y) \tag{21}$$

The clear sky planetary albedo feedback, $\lambda_{\text{albedo,ClearSky}}(x,y)$, is now evaluated by differentiating $\alpha_{\text{ClearSky}}$ with respect to surface temperature and substituting into the relevant term in Equations 17a and 17b. The partial derivative of local clear sky albedo respect to surface temperature is evaluated via,

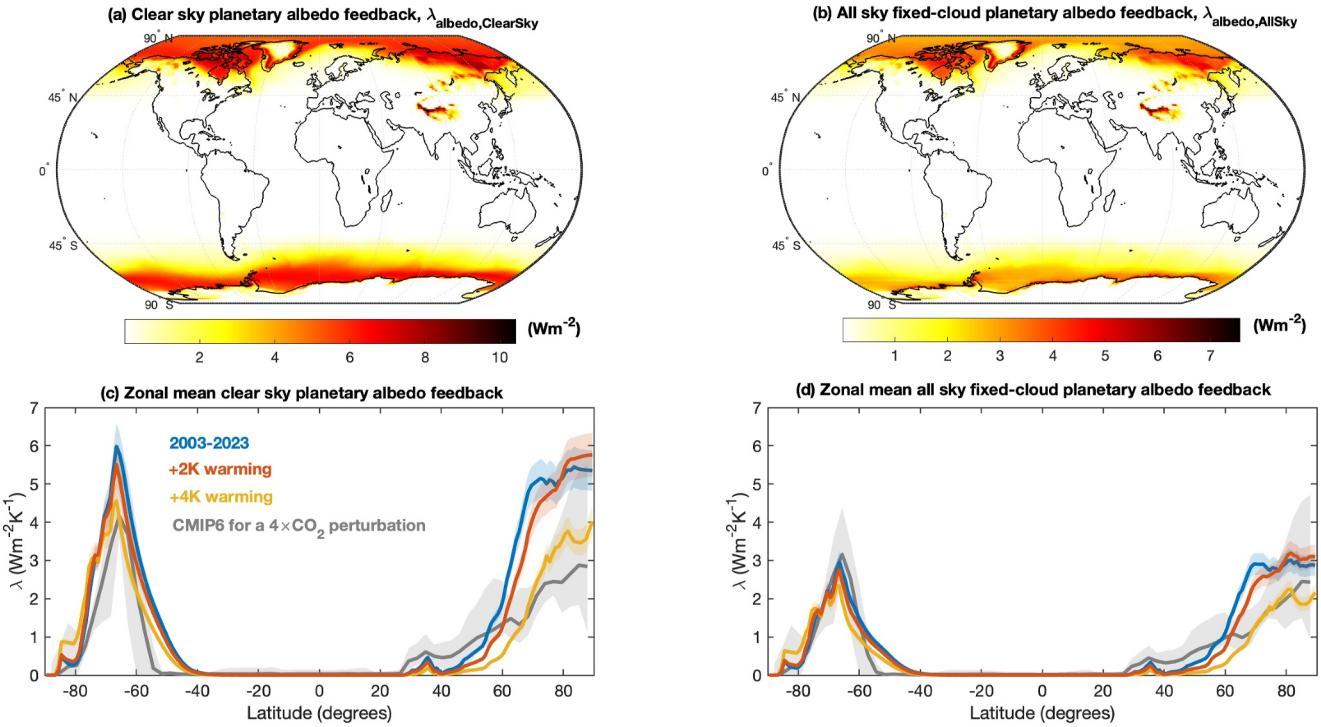



**Figure 7.** Clear sky and fixed-cloud planetary albedo feedback spatially and as a zonal average. The spatial planetary albedo feedback for the 2003–2023 period for (a) clear sky and (b) fixed-cloud all sky conditions. The zonal mean planetary albedo feedback for (c) clear sky and (d) fixed-cloud all sky conditions. Zonal mean feedbacks shown are for infinitesimal perturbation starting from the 2003–2023 climatology (blue), starting from a 2K warmed climate state (red) and starting from a 4K warmed climate state (orange). Zonal mean surface albedo feedback for finite 4xCO$_2$ perturbation is shown for CMIP6 models (gray), evaluated from radiative kernels for comparison.

$$\frac{\partial \alpha_{\text{ClearSky}}}{\partial T_S}(x,y) = \left[1+\beta\left[\frac{1}{2}\left[3\,\sin^2\phi - 1\right]\right]\right]\frac{\partial \overline{\alpha_{\text{ClearSky}}}}{\partial T_S}(x,y) \tag{22}$$

where $\frac{\partial \overline{\alpha_{\text{ClearSky}}}}{\partial T_S}(x,y)$ is the partial derivative of Equation 11 with respect to surface temperature, adopting the fitted parameter values over land and ocean (Table S1 in Supporting Information S1).

From our simplified relationships constrained by observed climatology for 2003–2023, the annual mean local clear sky albedo feedback (Equation 21: Figure 7a) reveals high values in the Himalayas and high latitude regions where a small temperature change would lead to a large variation in clear sky albedo. The zonal mean values evaluated from simplified empirical relations and observations here (Figure 7c, blue) show similarities to the values evaluated for CMIP6 models using radiative kernels following a 4xCO$_2$ perturbation (Figure 7c, gray), both in terms of the maximum magnitude and also the zonal pattern.

Three key differences arise from the spatially derived method used here (Figures 7a and 7c blue) compared to the standard temporally derived radiative kernel method applied to CMIP6 models (Figure 7c, gray):

1. The method here evaluates the feedback from observations within a reduced physics framework, whereas the radiative kernel method is applied to climate models that contain complex physics but may also contain model bias.
2. The method here implicitly considers the cryosphere and water vapor impacts on clear sky albedo, and does not consider any vegetation-induced albedo changes, whereas CMIP6 models with coupled vegetation will include both cryosphere and vegetation induced surface albedo changes but do not consider atmospheric water vapor absorption effects.
3. The method here evaluates $\lambda_{\text{albedo,ClearSky}}(x,y)$ for an infinitesimal perturbation to the climate state (Equation 21), whereas the radiative kernel approach applies to a large finite 4xCO$_2$ perturbation. Where snow or ice melts early in the large 4xCO$_2$ perturbation, this finite approximation will reduce the temporally derived



21698996, 2025, 12, Downloaded from https://agupubs.onlinelibrary.wiley.com/doi/10.1029/2024JD043186 by Imperial College London, Wiley Online Library on [19/10/2026]. See the Terms and Conditions (https://onlinelibrary.wiley.com/terms-and-conditions) on Wiley Online Library for rules of use; OA articles are governed by the applicable Creative Commons License

climate feedback relative to an infinitesimal perturbation, since the change in albedo will be the same but the change in the denominator (surface temperature) will be larger.

Anthropogenic forcing is warming future climate beyond an infinitesimal perturbation (IPCC, 2021). To explore large perturbations, our method evaluates $\lambda_{\text{albedo,ClearSky}}(x,y)$ for infinitesimal perturbations applied to warmed climate states, using surface temperature patterns for +2K and +4K global mean warming (IPCC, 2021) added on to the 1940–1960 climatological mean in the ERA5 surface temperature record (the earliest period within the ERA5 data set used). This choice results in reduced $\lambda_{\text{albedo,ClearSky}}(x,y)$ for the warmed climate states relative to the period 2003–2023, especially in northern high latitudes where the cryosphere is in retreat (Figure 7c, compare orange and red to blue). This response explains the higher $\lambda_{\text{albedo}}$ values obtained from our method relative to 4x$CO_2$ perturbation in CMIP6 models.

Uncertainties in $\lambda_{\text{albedo,ClearSky}}(x,y)$ are estimated from scaling arguments from the error in $\overline{\alpha_{\text{ClearSky}}}(x,y,T_S)$ divided by the range of $\overline{\alpha_{\text{ClearSky}}}(x,y,T_S)$: the fractional uncertainty in $\lambda_{\text{albedo,ClearSky}}(x,y)$ is estimated as the root mean square error in $\overline{\alpha_{\text{ClearSky}}}(x,y,T_S)$ divided by the maximum range of $\overline{\alpha_{\text{ClearSky}}}(x,y,T_S)$ over land and ocean (Figure 5c, blue, red, and orange shading).

To calculate the fixed-cloud planetary albedo feedback in all sky conditions, without considering changes in cloud amount or cloud properties,

$$\lambda_{\text{albedo,AllSky}} = -R_{\text{in}}\frac{\partial \alpha_{\text{AllSky}}}{\partial T_S} \tag{23}$$

we now calculate $\frac{\partial \alpha_{\text{AllSky}}}{\partial T_S}$, by considering the impact of cloudy skies and non-zero cloud amount on $\frac{\partial \alpha_{\text{ClearSky}}}{\partial T_S}$ (Equation 22). The partial derivative of cloudy sky albedo is related to the partial derivative of clear sky albedo via differentiating Equation 14 (Text S1 in Supporting Information S1),

$$\frac{\partial \alpha_{\text{CloudySky}}}{\partial T_S} = \left[\frac{\left[1-\alpha_{\text{Cloud;dir}}(x,y)\right]\left[1-\overline{\alpha_{\text{Cloud}}}\right]}{\left[1-\overline{\alpha_{\text{ClearSky}}}(x,y)\overline{\alpha_{\text{Cloud}}}\right]^2\left[1+\beta\left[0.5\times\left[3\,\sin^2\phi-1\right]\right]\right]}\right]\frac{\partial \alpha_{\text{ClearSky}}}{\partial T_S} \tag{24}$$

The partial derivatives of albedo with respect to surface temperature in clear sky, all sky and cloudy sky conditions are related, from Equation 7, via,

$$\frac{\partial \alpha_{\text{AllSky}}}{\partial T_S} = f_{\text{CI}}\frac{\partial \alpha_{\text{CloudySky}}}{\partial T_S} + \left[1-f_{\text{CI}}\right]\frac{\partial \alpha_{\text{ClearSky}}}{\partial T_S} \tag{25}$$

By substituting Equations 24 and 25 in Equations 17a and 17b the fixed-cloud planetary albedo feedback in all sky conditions becomes,

$$\lambda_{\text{albedo,AllSky}} = -R_{\text{in}}\left[f_{\text{CI}}\frac{\left[1-\overline{\alpha_{\text{Cloud}}}\right]\left[1-\alpha_{\text{Cloud;dir}}\right]}{\left[1-\overline{\alpha_{\text{ClearSky}}}\,\overline{\alpha_{\text{Cloud}}}\right]^2\left[1+\beta\left[0.5\times\left[3\,\sin^2\phi-1\right]\right]\right]}+\left[1-f_{\text{CI}}\right]\right]\frac{\partial \alpha_{\text{ClearSky}}}{\partial T_S} \tag{26}$$

The values of $\lambda_{\text{albedo,AllSky}}$ are calculated for surface temperatures during the period 2003–2023 (Figures 7b and 7d), and also for +2K and +4K warmed climate states (Figure 7d). The $\lambda_{\text{albedo,AllSky}}$ for each level of warming is correspondingly reduced relative to $\lambda_{\text{albedo,ClearSky}}$, and the $\lambda_{\text{albedo,AllSky}}$ values derived here from observations and simplified empirical relations are similar to the CMIP6 derived values using radiative kernels and a 4x$CO_2$ perturbation (Figure 7d). Uncertainty in $\lambda_{\text{albedo,AllSky}}$ is estimated through the application of the same scaling arguments as adopted for $\lambda_{\text{albedo,ClearSky}}$ (Figures 7c and 7d, blue, red, and orange shading).

The global mean fixed-cloud planetary albedo feedback in all sky conditions is 0.64 (0.58–0.70 at 66% confidence) $Wm^{-2}K^{-1}$ for 2003–2023 background surface temperatures, decreasing to 0.54 (0.49–0.59) $Wm^{-2}K^{-1}$ if background surface temperatures had already undergone +2K warming (Table 1) and decreasing to 0.35 (0.32–0.38) $Wm^{-2}K^{-1}$ for 4K warming. Note that a sensitivity study manually varying the value of $\beta$ in Equation 10 found that $\lambda_{\text{albedo,AllSky}}$ varied by only $\pm 0.05$ $Wm^{-2}K^{-1}$ when $\beta$ varied by $\pm 0.1$, which is 10 times the uncertainty



21698996, 2025, 12, Downloaded from https://agupubs.onlinelibrary.wiley.com/doi/10.1029/2024JD043186 by Imperial College London, Wiley Online Library on [19/10/2026]. See the Terms and Conditions (https://onlinelibrary.wiley.com/terms-and-conditions) on Wiley Online Library for rules of use; OA articles are governed by the applicable Creative Commons License

in $\beta(=0.33 \pm 0.01)$. Therefore, within uncertainty the value of $\beta$ does not significantly alter the fixed-cloud albedo within our spatial methodology.

### 3.3. Water Vapor Lapse Rate Feedback

The WVLR feedback is defined here as the change in outgoing longwave radiation per unit warming due to a change in the planetary emissivity of the atmosphere following a change in climate state. From Equations 17a and 17b the WVLR feedback for clear skies is,

$$\lambda_{\mathrm{WVLR,ClearSky}}(x,y) = -\sigma T_S^4(x,y)\frac{\partial \varepsilon_{\mathrm{ClearSky}}}{\partial T_S}(x,y) \tag{27}$$

We now need to evaluate $\frac{\partial \varepsilon_{\mathrm{ClearSky}}}{\partial T_S}$ by differentiating the observation-constrained reduced physics relation for $\varepsilon_{\mathrm{ClearSky}}$, Equation 13. Assuming that the changes in tropospheric height, mid-troposphere relative humidity, and surface pressure with a change in climate state alter planetary emissivity significantly less than the change in surface temperature, then the partial derivative becomes,

$$\frac{\partial \varepsilon_{\mathrm{ClearSky}}}{\partial T_S} \approx c_1 \tag{28}$$

This simplification is a good approximation so long as $\left|\frac{\partial z_{\mathrm{trop}}}{\partial T_S}\frac{\partial \varepsilon_{\mathrm{ClearSky}}}{\partial z_{\mathrm{trop}}}\right|$, $\left|\frac{\partial H_{\mathrm{rel}}}{\partial T_S}\frac{\partial \varepsilon_{\mathrm{ClearSky}}}{\partial H_{\mathrm{rel}}}\right|$ and $\left|\frac{\partial p_S}{\partial T_S}\frac{\partial \varepsilon_{\mathrm{ClearSky}}}{\partial p_S}\right|$ are each much smaller than $\left|\frac{\partial \varepsilon_{\mathrm{ClearSky}}}{\partial T_S}\right|$ (Equation 6), reflecting how the changes in tropospheric height, mid-troposphere relative humidity and surface pressure with a change in climate state alter planetary emissivity significantly less than the change in surface temperature.

Substituting Equation 28 into Equation 27, and using the constrained value of $c_1 = \frac{\partial \varepsilon_{\mathrm{ClearSky}}}{\partial T_S} = -(2.904 \pm 0.003) \times 10^{-3}$ $\mathrm{K}^{-1}$, gives $\lambda_{\mathrm{WVLR,ClearSky}}$ varying from approximately 0.5 $\mathrm{Wm}^{-2}\mathrm{K}^{-1}$ in cold regions to 1.5 $\mathrm{Wm}^{-2}\mathrm{K}^{-1}$ in warm regions (Figure 8, left hand column).

Uncertainty in the value of $\lambda_{\mathrm{WVLR,ClearSky}}$ is due to our assumption that $\varepsilon_{\mathrm{ClearSky}}$ is related to $T_S$ via a linear term in Equation 13, $c_1 T_S$. The observed relation between spatial variation in $\varepsilon_{\mathrm{ClearSky}}$ and $T_S$ in modern climatology does reveal an approximate linear relation (Figure 4e), which informs the decision to assume a linear term in Equation 13 as a best estimate for the functional relationship. However, a nonlinear relationship is still possible. Text S2 Supporting Information S1 evaluates the uncertainty in $\lambda_{\mathrm{WVLR,ClearSky}}$ that arises from the introduction of a nonlinear term between $\varepsilon_{\mathrm{ClearSky}}$ and $T_S$ via modification of Equation 13, whereby the $c_1 T_S$ term becomes $c_1 T_S^n$. The systematic uncertainty in $\lambda_{\mathrm{WVLR,ClearSky}}$ arising from the linear assumption is evaluated in assuming that the value of the power varies with a normal distribution with mean 1 and standard deviation 1, $n \sim N(1,1)$ (Text S2 in Supporting Information S1; Figure 8c, blue shading). The relatively small systematic uncertainty introduced by the linear assumption (Figure 8c), combined with the good statistical fit for Equation 13 (Figure 2; Table S2 in Supporting Information S1), provides confidence in the evaluation of $\lambda_{\mathrm{WVLR,ClearSky}}$ (Figures 8a and 8c).

The WVLR feedback in all sky conditions is given by,

$$\lambda_{\mathrm{WVLR,AllSky}}(x,y) = -\sigma T_S^4(x,y)\frac{\partial \varepsilon_{\mathrm{AllSky}}}{\partial T_S}(x,y) \tag{29}$$

where it is assumed that both cloud amount, $f_{\mathrm{CA}}$, and cloud type are unchanging with perturbation. The impact on outgoing longwave radiation of cloud type is represented in this study by the cloud-emissivity coefficient, $c_\varepsilon$ (Equation 16; Goodwin and Williams, 2023) in Equation 15, relating $\varepsilon_{\mathrm{AllSky}}$ to $\varepsilon_{\mathrm{ClearSky}}$, $f_{\mathrm{CA}}$ and $c_\varepsilon$. Therefore, to identify $\frac{\partial \varepsilon_{\mathrm{AllSky}}}{\partial T_S}(x,y)$ as a function of $\frac{\partial \varepsilon_{\mathrm{ClearSky}}}{\partial T_S}(x,y)$, we differentiate Equation 15 with respect to surface temperature holding $f_{\mathrm{CA}}$ and $c_\varepsilon$ constant to reveal,

$$\frac{\partial \varepsilon_{\mathrm{AllSky}}}{\partial T_S}(x,y) = \left[1 - f_{\mathrm{CA}}(x,y) + f_{\mathrm{CA}}(x,y)\, c_\varepsilon(x,y)\right]\frac{\partial \varepsilon_{\mathrm{ClearSky}}}{\partial T_S}(x,y) \tag{30}$$



21698996, 2025, 12, Downloaded from https://agupubs.onlinelibrary.wiley.com/doi/10.1029/2024JD043186 by Imperial College London, Wiley Online Library on [19/10/2026]. See the Terms and Conditions (https://onlinelibrary.wiley.com/terms-and-conditions) on Wiley Online Library for rules of use; OA articles are governed by the applicable Creative Commons License

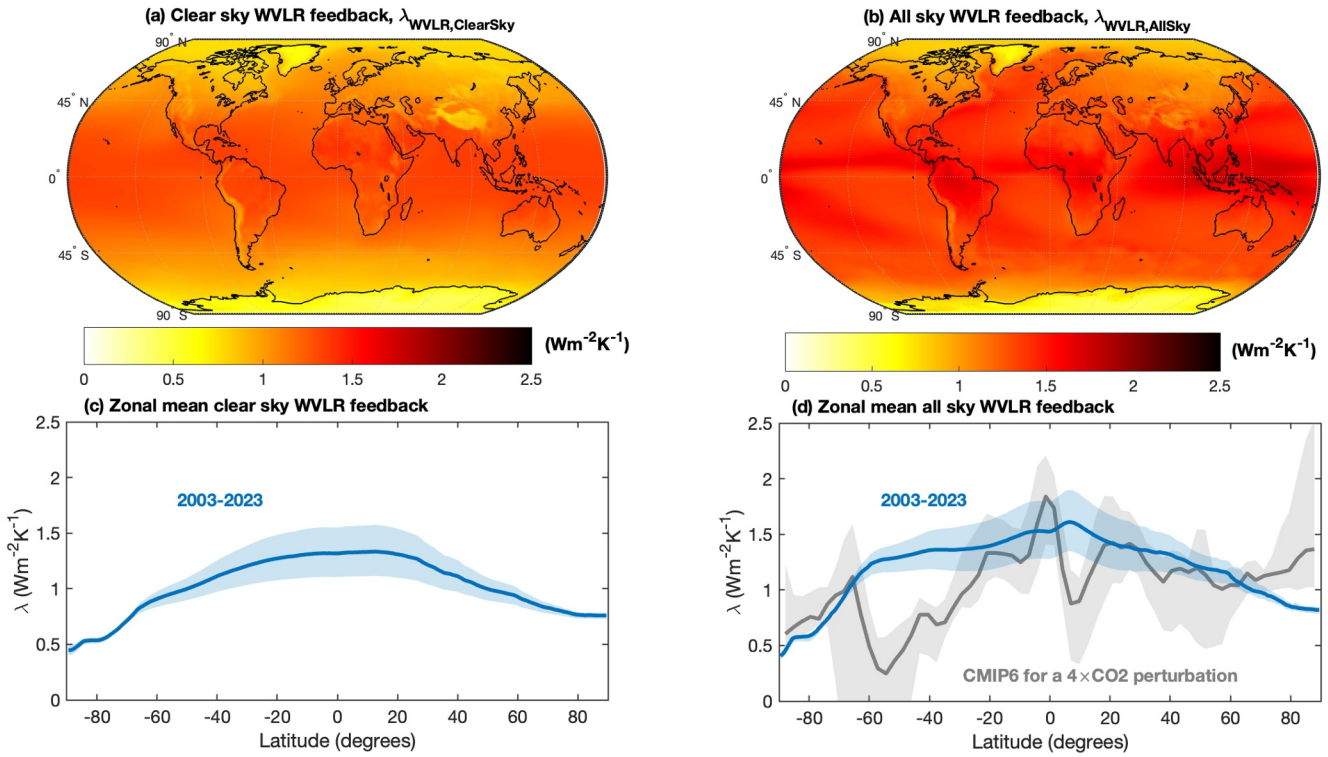



**Figure 8.** The water vapor-lapse rate (WVLR) feedback spatially and as a zonal average for clear sky and all sky conditions. The spatial WVLR feedback for the 2003–2023 period for (a) clear sky and (b) all sky conditions. The zonal mean WVLR feedback for (c) clear sky and (d) all sky conditions. Zonal mean feedbacks shown are for infinitesimal perturbation starting from the 2003–2023 climatology (blue) and for finite 4x$CO_2$ perturbation for CMIP6 models (gray), evaluated from radiative kernels.

Substituting Equation 30 into Equation 29 then reveals the WVLR feedback in all sky conditions in terms of the sensitivity of clear sky planetary emissivity to surface temperature, the cloud amount area fraction, the cloud-emissivity coefficient, surface temperature and the Stefan-Boltzmann constant,

$$\lambda_{\mathrm{WVLR,AllSky}}(x,y) = -\sigma T_S^4\left[1 - f_{\mathrm{CA}} + f_{\mathrm{CA}} c_\varepsilon\right]\frac{\partial \varepsilon_{\mathrm{ClearSky}}}{\partial T_S}(x,y) \tag{31}$$

This relation is evaluated for the observed climatology from 2003 to 2023, revealing $\lambda_{\mathrm{WVLR,AllSky}}$ spatially (Figure 8b) and for zonal averages (Figure 8d), where zonal averages include the systematic uncertainty from the assumption of a linear term relating $\varepsilon_{\mathrm{ClearSky}}$ and $T_S$ (Figure 8d, blue shading; Text S2 in Supporting Information S1). The magnitudes of zonal average $\lambda_{\mathrm{WVLR,AllSky}}$ are generally similar to CMIP6 model values approximated through radiative kernels and a 4x$CO_2$ temporal perturbation (Figure 8d), but show a smoother latitudinal variation. This may reflect a difference between how cloud amount and type are held constant between the methodologies ($\delta c_\varepsilon = 0$ and $\delta f_{\mathrm{CA}} = 0$ here vs. imposed constant simulated cloud amount and type in the CMIP6 simulations). These different methodologies may then imply differences in how clouds interact with non-cloud features of the air column that are changing with perturbation (e.g., water vapor content and aerosols) to affect longwave radiation.

The global mean all sky WVLR feedback is 1.28 (1.13–1.45) Wm$^{-2}$K$^{-1}$ for the 2003–2023 surface temperatures (Table 1). Our analysis suggests that the WVLR feedback only increases a small amount as the world warms, although we note that we do not have a strong constraint on the second derivative of planetary emissivity with surface temperature from our observationally constrained functional relationship (Equation 13, Text S2 in Supporting Information S1). Therefore, we have low confidence in the WVLR feedback evaluation for the +2 K and +4 K warmed worlds. When comparing to other studies, note that our methodology includes only the LW component of the WVLR feedback (Table 1), the SW component arising from changes in water vapor absorbing or scattering SW radiation is implicitly included within our clear sky and fixed-cloud planetary albedo feedbacks.



21698996, 2025, 12, Downloaded from https://agupubs.onlinelibrary.wiley.com/doi/10.1029/2024JD043186 by Imperial College London, Wiley Online Library on [19/10/2026]. See the Terms and Conditions (https://onlinelibrary.wiley.com/terms-and-conditions) on Wiley Online Library for rules of use; OA articles are governed by the applicable Creative Commons License

21698996, 2025, 12, Downloaded from https://agupubs.onlinelibrary.wiley.com/doi/10.1029/2024JD043186 by Imperial College London, Wiley Online Library on [19/10/2026]. See the Terms and Conditions (https://onlinelibrary.wiley.com/terms-and-conditions) on Wiley Online Library for rules of use; OA articles are governed by the applicable Creative Commons License

Note also the similarity between our estimate and temporally derived estimates arises even though not all processes that act temporally may be included within the spatial analysis used to constrain WVLR here (see Section 2.2.2 above).

### 3.4. Global Mean Total Feedback

The global mean values of the Planck, WVLR and fixed-cloud planetary albedo feedbacks are analyzed from spatial variation for the 2003–2023 climatology combined with a +2K warming pattern (Table 1), and are similar in magnitude to values analyzed using temporal perturbation methods (IPCC, 2021; Sherwood et al., 2020; Zelinka et al., 2020). Although the Planck and WVLR feedbacks are consistent (Table 1), the fixed-cloud planetary albedo feedback for the 2003–2023 climatology is larger than recent estimates for surface albedo from temporal variation by around 0.3 $Wm^{-2}K^{-1}$. Two possible reasons for this include: Firstly, our fixed-cloud planetary albedo estimate implicitly includes both how surface albedo changes with temperature from the cryosphere and how atmospheric albedo changes with temperature from WVLR effects. These shortwave WVLR effects are not included within estimates of surface albedo (IPCC, 2021; Sherwood et al., 2020; Zelinka et al., 2020) but are estimated at around 0.3 $Wm^{-2}K^{-1}$ (Donohoe et al., 2014). Note this also implies that our WVLR feedback is actually more consistent with the Sherwood et al. (2020) estimate, since we do not include the shortwave component (Table 1). Secondly, our fixed-cloud albedo estimate is calculated for an infinitesimal perturbation to the 2003–2023 climatology, whereas previous surface albedo estimates are calculated for a large 4xCO2 perturbation. Our albedo estimate becomes more consistent with previous estimates when the world has warmed by +2K and +4K above the mid-20th century average.

To calculate total climate feedback, $\lambda_{total} = \Sigma\lambda_X$, we combine our Planck, WVLR and fixed-cloud planetary-albedo feedback estimates in all sky conditions with two estimates of cloud feedback: Ceppi and Nowack (2021): $\lambda_{cloud} = 0.43 \pm 0.35$ $Wm^{-2}K^{-1}$ at 90% confidence that applies after a $4xCO_2$ perturbation after surface warming patterns have adjusted; and Raghuraman et al. (2023) $\lambda_{cloud} = 0.20 \pm 0.34$ $Wm^{-2}K^{-1}$ at 95% confidence that applies in the present climate state before any future adjustments to surface warming patterns. Note that these cloud feedback estimates are similar to estimates from recent reviews of the literature (IPCC, 2021; Sherwood et al., 2020; Table 1), with Ceppi and Nowack (2021) toward the more amplifying range and Raghuraman et al. (2023) toward the less amplifying range. We calculate the total global mean climate feedback only for the 2003–2023 climatology, since we have low confidence in the WVLR feedbacks for the +2 and + 4 K warmed worlds (Table 1). Assuming independent uncertainty between terms, our analysis combined with Ceppi and Nowack (2021) provides a $\lambda_{total} = -0.95$ [−0.49 to −1.40 at 90% confidence] $Wm^{-2}K^{-1}$ for the period 2003–2023 (Table 1; Figure 8a), whereas when combined with Raghuraman et al. (2023) we find $\lambda_{total} = -1.18$ [−0.77 to −1.58] $Wm^{2}K^{-1}$. Our spatially derived estimates are consistent with previous temporal variation methods for calculating total climate feedback (Figure 9; Table 1: IPCC, 2021; Sherwood et al., 2020; Zelinka et al., 2020), with the choice of cloud feedback determining whether our best estimate is more similar to the mean of the CMIP6 models or the IPCC (2021) AR6 (Table 1), although noting that the Ceppi and Nowack (2021) cloud feedback estimate applies after a $4xCO_2$ perturbation and so is more directly relevant as a comparison to the previous net climate feedback estimates (Table 1). Note that in the Sherwood et al. (2020) review, additional evidence is used to constrain ECS that is not used to constrain the climate feedback, and therefore the reduced range of our $\lambda_{total}$ estimate relative to Sherwood et al. (2020) (Figure 9) does not imply a similarly reduced range for ECS.

## 4. Discussion

Many existing methods evaluate climate feedbacks from the *temporal* variation in climate state following some perturbation (e.g., Sherwood et al., 2020). When applied to numerical climate models, the temporal variation is induced by application of finite perturbations to the climate system, often with a quadrupling of atmospheric $CO_2$ (e.g., Soden et al., 2008; Zelinka et al., 2020). Observation-based methods (e.g., Cael et al., 2023; Goodwin, 2021; Goodwin and Cael, 2021; Sherwood et al., 2020) often employ the recent temporal changes in surface temperature and outgoing radiation at TOA, where time-mean net outgoing radiation is sometimes deduced from heat content changes in the ocean and Earth system. Paleoclimate approaches avoid the need to calculate Earth's transient energy imbalance by considering longer timescales, but do rely on proxy evidence to reconstruct the observable quantities (e.g., Rohling et al., 2018). Other approaches involving observational records include using the internal variability within observational records to constrain climate feedback (Dessler, 2013) and applying emergent

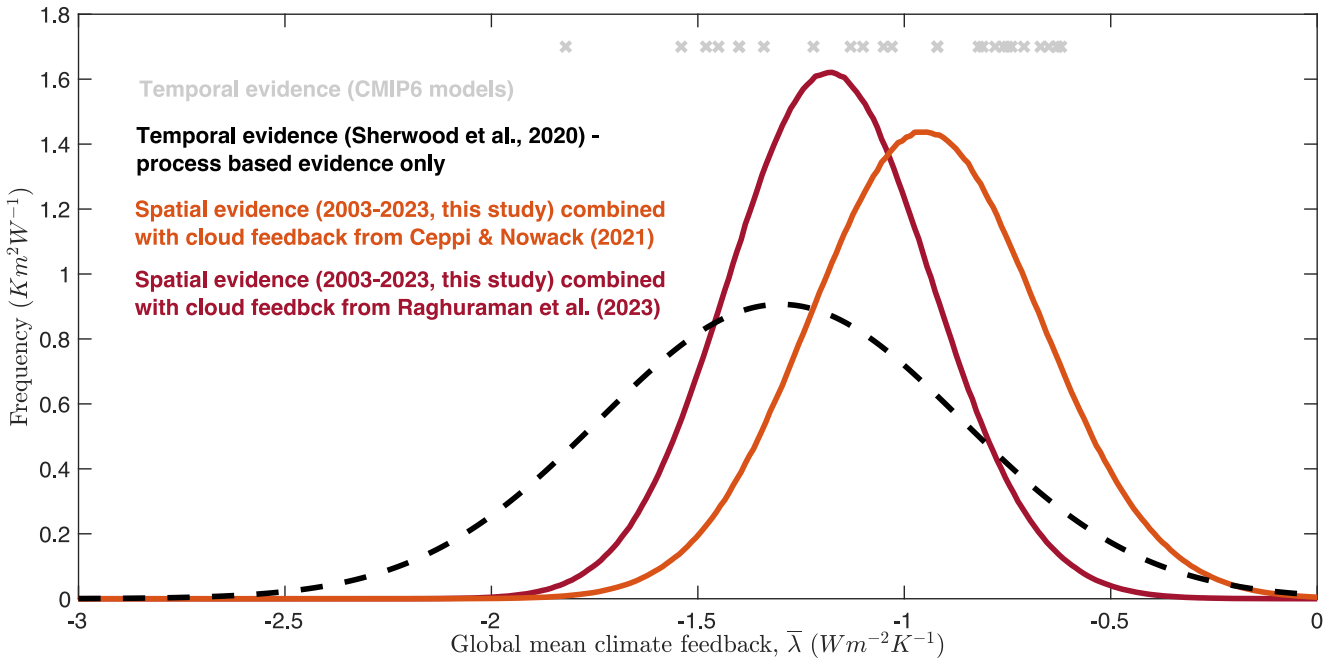



**Figure 9.** Frequency distributions for effective global mean climate feedback, and values for individual CMIP6 models. Shown are constraints from spatial evidence from this study (red and dark red lines), and externally calculated temporal evidence values including for CMIP6 models (gray crosses: Zelinka et al., 2020), and from a recent review (black dashed line: Sherwood et al., 2020).

constraints to assess which complex climate models have the best simulated representation of the climate's sensitivity to change (e.g., Cox et al., 2018).

This study has presented a new methodology for evaluating climate feedbacks, where simplified relations between outgoing radiation and climatological properties (Equations 1–30) are empirically constrained with *spatial* variation in observed climatology (Hersbach et al., 2023; Loeb et al., 2018; Figures 1–6), and then differentiated with respect to surface temperature to reveal the Planck, WVLR and fixed-cloud planetary albedo feedbacks (Figures 7 and 8). The climate feedbacks are evaluated spatially at 1° by 1° horizontal resolution, and then a global mean is found by convoluting with a spatial warming pattern.

When spatial variation is considered, both TOA outgoing longwave radiation and outgoing shortwave radiation vary considerably with surface temperature (e.g., Figures 2c and 2d for clear skies), which is expressed via spatial variation in planetary emissivity and planetary albedo respectively (Figures 2e and 2f). Our simplified and empirically constrained relations identify that 91% of the apparent spatial link between clear sky albedo and surface temperature arises through a functional dependence. The remaining 9% of the apparent spatial link arises through the latitudinal effect on the solar-zenith angle, which co-varies with surface temperature in space but would not co-vary with temperature in time following perturbation. Similarly, we identify that around 77% of the apparent spatial link between clear sky planetary emissivity and surface temperature arises through a functional dependence. The remaining 23% of this apparent spatial link arises through factors that co-vary with surface temperature in space but would not co-vary in time following perturbation, such as surface pressure and the height of the tropopause. Through extracting these co-varying factors, our methodology uses observed spatial variation in outgoing radiation and surface temperature to evaluate climate feedbacks following perturbation.

Our spatial-variation methodology is complementary to existing temporal-variation methods, with consistent results (Table 1) derived from independent evidence, assumptions and uncertainties. For example, the reduced physics nature of our approach contrasts with the complex climate models used for evaluating climate feedbacks in the literature (e.g., Zelinka et al., 2020). However, the ability to evaluate climate feedbacks from spatial variation in observed climatology produces a significantly better signal-to-noise ratio (with spatial temperatures and outgoing radiation varying by order 80 K and 100 $Wm^{-2}K^{-1}$ respectively) when compared to historic observations of temporal changes in temperature and outgoing radiation (of order 1 K and 1 $Wm^{-2}K^{-1}$



21698996, 2025, 12, Downloaded from https://agupubs.onlinelibrary.wiley.com/doi/10.1029/2024JD043186 by Imperial College London, Wiley Online Library on [19/10/2026]. See the Terms and Conditions (https://onlinelibrary.wiley.com/terms-and-conditions) on Wiley Online Library for rules of use; OA articles are governed by the applicable Creative Commons License

21698996, 2025, 12, Downloaded from https://agupubs.onlinelibrary.wiley.com/doi/10.1029/2024JD043186 by Imperial College London, Wiley Online Library on [19/10/2026]. See the Terms and Conditions (https://onlinelibrary.wiley.com/terms-and-conditions) on Wiley Online Library for rules of use; OA articles are governed by the applicable Creative Commons License

respectively). When producing an estimate of climate feedback, and the related ECS, from multiple lines of evidence using a Bayesian framework then a method that is largely independent of preexisting methods can be useful in narrowing the overall uncertainty range (Sherwood et al., 2020), such as the method presented here (e.g., Figure 9).

Our best estimate for global mean total climate feedback analyzed from spatial information, comes out similar in magnitude to the IPCC (2021) AR6 and Sherwood et al. (2020) estimates, depending on the independent cloud feedback estimate used (Table 1). One difference in methodology is that our spatial estimate considers the albedo feedback for an infinitesimal warming perturbation, whereas the IPCC (2021) and Sherwood et al. (2020) estimates consider a $4xCO_2$ perturbation with relatively large finite warming. When we apply our methodology to calculate the albedo feedback for infinitesimal perturbation starting from a warmed world (Table 1; Figure 7), there is a reduction in the positive albedo feedback by a magnitude enough to explain the difference between our estimate of total climate feedback and the IPCC (2021) and Sherwood et al. (2020) estimates.

## Conflict of Interest

The authors declare no conflicts of interest relevant to this study.

## Data Availability Statement

The ERA5 reanalysis (Hersbach et al., 2023) for monthly averaged data on single levels is available for download here: https://doi.org/10.24381/cds.f17050d7 (accessed 31-03-2024). The CERES Energy Balanced and filled (EBAF4.2) satellite observation data set used here for the period 2003–2023 (Loeb et al., 2018) is available here: https://doi.org/10.5067/TERRA-AQUA-NOAA20/CERES/EBAF-TOA_L3B004.2 (accessed 08/04/2024; data set reference: NASA/LARC/SD/ASDC (2022)). CMIP data were obtained from the UK Centre for Environmental Data Analysis portal (https://esgf-index1.ceda.ac.uk/search/cmip6-ceda/; data set reference WCRP (2024)). We acknowledge the WCRP, which, through its Working Group on Coupled Modeling, coordinated and promoted CMIP6. We thank the climate-modeling groups for producing and making available their model output, the Earth System Grid Federation (ESGF) for archiving the data and providing access and the multiple funding agencies that support CMIP6 and ESGF. Code for calculating the height of the tropopause, from Mateus et al. (2022), is available for download here: https://github.com/pjmateus/global_tropopause_model (accessed 14/04/2023, Model code reference Mateus et al. (2022b)); where this study uses the options for a bilinear interpolation model of the tropopause, and a surface at 3.0 potential vorticity units, where 1 potential vorticity unit is equal to $10^{-6}$ K kg$^{-1}$ m$^2$ s$^{-1}$. The GMTED2010 data set for mean surface elevation (Danielson & Gesch, 2011) is available here: https://temis.nl/data/gmted2010/ (accessed 18/03/2024; Data set reference USGS (2011)). The MATLAB code developed here for conducting the analysis here is available at https://github.com/WASP-ESM/Spatial_Climate_Feedback/tree/main (model code reference Goodwin et al. (2025) https://doi.org/10.5281/zenodo.15624497). Note that the code requires separate download of data sets mentioned above.

**Acknowledgments**
The authors are thankful for the support from UKRI NERC, Grant Number: NE/T010657/1.

## References

Cael, B. B., Bloch-Jonhson, J., Ceppi, P., Fredriksen, H.-B., Goodwin, P., Gregory, J. M., et al. (2023). Energy budget diagnosis of changing climate feedback. *Science Advances*, *9*(16), eadf9302. https://doi.org/10.1126/sciadv.adf9302

Ceppi, P., & Nowack, P. (2021). Observational evidence that cloud feedback amplifies global warming. *Proceedings of the National Academy of Sciences of the United States of America*, *118*(30), e2026290118. https://doi.org/10.1073/pnas.2026290118

Cox, P., Huntingford, C., & Williamson, M. (2018). Emergent constraint on equilibrium climate sensitivity from global temperature variability. *Nature*, *553*(7688), 319–322. https://doi.org/10.1038/nature25450

Cronin, T. W. (2014). On the choice of average solar zenith angle. *Journal of the Atmospheric Sciences*, *71*(8), 2994–3003. https://doi.org/10.1175/JAS-D-13-0392.1

Danielson, J. J., & Gesch, D. B. (2011). *Global multi-resolution terrain elevation data 2010 (GMTED2010)* (Vol. 1073). U.S. Geological Survey Open-File Report.26

Dessler, A. E. (2013). Observations of climate feedbacks over 2000–10 and comparisons to climate models. *Journal of Climate*, *26*(1), 333–342. https://doi.org/10.1175/JCLI-D-11-00640.1

Donohoe, A., Armour, K. C., Pendergrass, A. G., & Battisti, D. S. (2014). Shortwave and longwave radiative contributions to global warming under increasing CO2. *Proceedings of the National Academy of Sciences of the United States of America*, *111*(47), 16700–16705. https://doi.org/10.1073/pnas.1412190111

Feldl, N., & Merlis, T. M. (2023). A semi-analytical model for water vapor, temperature, and surface-albedo feedbacks in comprehensive climate models. *Geophysical Research Letters*, *50*, e2023GL105796. https://doi.org/10.1029/2023GL105796

Feng, J., Paynter, D., & Menzel, R. (2023a). How a stable greenhouse effect on Earth is maintained under global warming. *Journal of Geophysical Research: Atmospheres*, *128*(9), e2022JD038124. https://doi.org/10.1029/2022jd038124

Feng, J., Paynter, D., Wang, C., & Menzel, R. (2023b). How atmospheric humidity drives the outgoing longwave radiation-surface temperature relationship and inter-model spread. *Environmental Research Letters*, *18*(10), 104033. https://doi.org/10.1088/1748-9326/acfb98

Goodwin, P. (2021). Probabilistic projections of future warming and climate sensitivity trajectories. *Oxford Open Climate Change*, *1*(1), kgab007. https://doi.org/10.1093/oxfclm/kgab007

Goodwin, P., & Cael, B. B. (2021). Bayesian estimation of Earth's climate sensitivity and transient climate response from observational warming and heat content datasets. *Earth System Dynamics*, *12*(2), 709–723. https://doi.org/10.5194/esd-12-709-2021

Goodwin, P., & Williams, R. G. (2023). On the Arctic Amplification of surface warming in a conceptual climate model. *Physica D: Nonlinear Phenomena*, *454*, 133880. https://doi.org/10.1016/j.physd.2023.133880

Goodwin, P., Williams, R. G., Ceppi, P., & Cael, B. B. (2025). Spatial climate feedbacks derived from spatial gradients in recent climatology model code [model code]. https://doi.org/10.5281/zenodo.15624497

Gregory, J. M., & Andrews, T. (2016). Variation in climate sensitivity and feedback parameters during the historical period. *Geophysical Research Letters*, *43*(8), 3911–3920. https://doi.org/10.1002/2016GL068406

Hartmann, D. L. (1994). *Global Physical Climatology*. Academic Press.411

Hersbach, H., Bell, B., Berrisford, P., Biavati, G., Horányi, A., Muñoz Sabater, J., et al. (2023). ERA5 monthly averaged data on single levels from 1940 to present [Dataset]. *Copernicus Climate Change Service (C3S) Climate Data Store (CDS)*. https://doi.org/10.24381/cds.f17050d7

Ingram, W. (2010). A very simple model for the water vapour feedback on climate change. *Quarterly Journal of the Royal Meteorological Society*, *136*(646), 30–40. https://doi.org/10.1002/qj.546

IPCC. (2021). In V. Masson-Delmotte, P. Zhai, A. Pirani, S. L. Connors, C. Péan, et al. (Eds.), *Climate Change 2021: The Physical Science Basis. Contribution of Working Group I to the Sixth Assessment Report of the Intergovernmental Panel on Climate Change*. Cambridge University Press. https://doi.org/10.1017/9781009157896

Koll, D. D., Jeevanjee, N., & Lutsko, N. J. (2023). An analytic model for the clear-sky longwave feedback. *Journal of the Atmospheric Sciences*, *80*(8), 1923–1951. https://doi.org/10.1175/JAS-D-22-0178.1

Koll, D. D. B., & Cronin, T. W. (2018). Earth's outgoing longwave radiation linear due to $H_2O$ greenhouse effect. *Proceedings of the National Academy of Sciences of the United States of America*, *115*(41), 10293–10298. https://doi.org/10.1073/pnas.1809868115

Loeb, N. G., Doelling, D. R., Wang, H., Su, W., Nguyen, C., Corbett, J. G., et al. (2018). Clouds and the earth's radiant energy system (CERES) energy balanced and filled (EBAF) top-of-atmosphere (TOA) edition-4.0 data product. *Journal of Climate*, *31*(2), 895–918. https://doi.org/10.1175/JCLI-D-17-0208.1

Mateus, P., Mendes, V. B., & Pires, C. A. L. (2022). Global empirical models for tropopause height determination. *Remote Sensing*, *14*(17), 4303. https://doi.org/10.3390/rs14174303

Mateus, P., Mendes, V. B., & Pires, C. A. L. (2022b). Global tropopause models. [model code]. *Remote Sensing*, *14*(17), 4303. https://doi.org/10.3390/rs14174303

NASA/LARC/SD/ASDC. (2022). CERES energy balanced and filled (EBAF) TOA monthly means data in netCDF Edition4.2 [Dataset]. *NASA Langley Atmospheric Science Data Center DAAC*. https://doi.org/10.5067/TERRA-AQUA-NOAA20/CERES/EBAF-TOA_L3B004.2

Payne, R. E. (1972). Albedo of the sea surface. *Journal of the Atmospheric Sciences*, *25*(5), 959–970. https://doi.org/10.1175/1520-0469(1972)029<0959:AOTSS>2.0.CO;2

Pincus, R., Mlawer, E. J., Oreopoulos, L., Ackerman, A. S., Baek, S., Brath, M., et al. (2015). Radiative flux and forcing parameterization error in aerosol-free clear skies. *Geophysical Research Letters*, *42*(13), 5485–5492. https://doi.org/10.1002/2015GL064291

Raghuraman, S. P., Paynter, D., Menzel, R., & Ramaswamy, V. (2023). Forcing, cloud feedbacks, cloud masking, and internal variability in the cloud radiative effect satellite record. *Journal of Climate*, *36*(12), 4151–4167. https://doi.org/10.1175/JCLI-D-22-0555.1

Raval, A., & Ramanathan, V. (1989). Observational determination of the greenhouse effect. *Nature*, *342*(6251), 758–761. https://doi.org/10.1038/342758a0

Roemer, F. E., Buehler, S. A., Brath, M., Kluft, L., & John, V. O. (2023). Direct observation of Earth's spectral long-wave feedback parameter. *Nature Geoscience*, *16*(5), 416–421. https://doi.org/10.1038/s41561-023-01175-6

Rohling, E. J., Marino, G., Foster, G. L., Goodwin, P. A., von der Heydt, A. S., & Köhler, P. (2018). Comparing climate sensitivity, past and present. *Annual Review of Marine Science*, *10*, 261–288. https://doi.org/10.1146/annurev-marine-121916-063242

Schmidt, G. A., Ruedy, R., Miller, R. L., & Lacis, A. A. (2010). Attribution of the present-day total greenhouse effect. *Journal of Geophysical Research*, *115*(D20), D20106. https://doi.org/10.1029/2010JD014287

Sherwood, S. C., Webb, M. J., Annan, J. D., Armour, K. C., Forster, P. M., Hargreaves, J. C., et al. (2020). An assessment of Earth's climate sensitivity using multiple lines of evidence. *Reviews of Geophysics*, *58*(4), e2019RG000678. https://doi.org/10.1029/2019RG000678

Soden, B. J., Held, I. M., Colman, R., Shell, K. M., Kiehl, J. T., & Shields, C. A. (2008). Quantifying climate feedbacks using radiative kernels. *Journal of Climate*, *21*(14), 3504–3520. https://doi.org/10.1175/2007JCLI2110.1

Stephens, G. L. (1978). Radiation profiles in extended water clouds. II: Parameterization schemes. *Journal of the Atmospheric Sciences*, *35*(11), 2123–2132. https://doi.org/10.1175/1520-0469(1978)035<2123:RPIEWC>2.0.CO;2

Taylor, K. E., Crucifix, M., Braconnot, P., Hewitt, C. D., Doutriaux, C., Broccoli, A. J., et al. (2007). Estimating shortwave radiative forcing and response in climate models. *Journal of Climate*, *20*(11), 2530–2543. https://doi.org/10.1175/JCLI4143.1

USGS. (2011). GMTED2010 global digital elevation model [Dataset]. *USGS*. Retrieved from https://temis.nl/data/gmted2010/

WCRP. (2024). Coupled model intercomparison project (Phase 6) [Dataset]. *WCRP*. Retrieved from https://esgf-index1.ceda.ac.uk/search/cmip6-ceda/

Zelinka, M. D., Myers, T. A., McCoy, D. T., Po-Chedley, S., Caldwell, P. M., Ceppi, P., et al. (2020). Causes of higher climate sensitivity in CMIP6 models. *Geophysical Research Letters*, *47*(1), e2019GL085782. https://doi.org/10.1029/2019GL085782



21698996, 2025, 12, Downloaded from https://agupubs.onlinelibrary.wiley.com/doi/10.1029/2024JD043186 by Imperial College London, Wiley Online Library on [19/10/2026]. See the Terms and Conditions (https://onlinelibrary.wiley.com/terms-and-conditions) on Wiley Online Library for rules of use; OA articles are governed by the applicable Creative Commons License